This is the peer-reviewed, final accepted version for American Mineralogist, published by the Mineralogical Society of America.
The published version is subject to change. Cite as Authors (Year) Title. American Mineralogist, in press.
DOI: https://doi.org/10.2138/am-2021-7828. http://www.minsocam.org/

Revision 1

Reduction of Structural Fe(III) in Nontronite by Humic Substances in the Absence and Presence of *Shewanella putrefaciens* and Accompanying Secondary Mineralization

Running title: Bioreduction of Nontronite in the Presence of Humic Acid

Hongyan Zuo[a], Liuqin Huang[b] Rosalie K. Chu[c], Nikola Tolic[c], Nancy Washton[c], Zihua Zhu[c], Richard E. Edelmann[d], Samar Elagamy[e], Andre Sommer[e], Fubo Luan[f], Qiang Zeng[g], Yu Chen[g], Dafu Hu[g], Di Zhan[g], Jinglong Hu[g], and Hailiang Dong[a,g*]

[a]Department of Geology and Environmental Earth Science, Miami University, Oxford, OH 45056, USA

[b]State Key Laboratory of Biogeology and Environmental Geology, China University of Geosciences, Wuhan, 430074, China

[c]Environmental Molecular Sciences Laboratory, Pacific Northwest National Laboratory, Richland, Washington 99354, USA

[d]Center for Advanced Microscopy & Imaging, Miami University, Oxford, OH 45056, USA

[e]Molecular Microspectroscopy Laboratory, Department of Chemistry and Biochemistry, Miami University, Oxford, OH 45056, USA

[f]Research Center for Eco-Environmental Sciences, Chinese Academy of Sciences, Beijing, 100085, China

[g]State Key Laboratory of Biogeology and Environmental Geology, China University of Geosciences, Beijing 100083, China

Revised for American Mineralogist, December 23, 2020

ABSTRACT

Studies have shown the electron shuttling role of humic substances (HS) in enhancing microbial reduction of solid-phase Fe(III), but it is unknown if native HS can reduce structural Fe(III) in clays, and how their chemical properties affect this process and secondary mineralization. The objective of this study was to evaluate the role of natural HS, Leonardite humic acid (LHA) and Pahokee Peat humic acid (PPHA), in reducing structural Fe(III) in nontronite with or without *Shewanella putrefaciens*. The extent of Fe(III) reduction was determined with a wet chemical method. Electrochemical method, spectroscopy, and mass spectrometry were used to determine the changes of HS electrochemical and molecular composition after bioreduction. X-ray diffraction and electron microscopy were used to observe mineralogical transformations. The results showed that natural HS not only served as electron donor to abiotically reduce Fe(III) in nontronite, but also served as electron shuttle to enhance Fe(III) bioreduction by *S. putrefaciens*. In the presence of CN32 cells, both the rate and extent of Fe(III) reduction significantly increased. Between the two HS, PPHA was more effective. The final bioreduction extent was 12.2% and 17.8% with LHA and PPHA, respectively, in bicarbonate buffer. Interestingly, when CN32 cells were present, LHA and PPHA donated more electrons to NAu-2, suggesting that CN32 cells were able to make additional electrons of LHA and PPHA available to reduce structural Fe(III). Though LHA reduced less Fe(III), it induced more extensive mineral transformation. In contrast, PPHA reduced more Fe(III), but did not induce any mineralogical change. These contrasting behaviors between two humic acids are ascribed to their differences in electron donating capacity, reactive functional group distribution, and metal

complexation capacity. A unique set of secondary minerals, including talc, illite, silica, albite, ilmenite, and ferrihydrite formed as a result of reduction. The results highlight the importance of coupled C and Fe biogeochemical transformations and have implications for nutrient cycling and contaminant migration in the environment.

Key words: LHA, Mineralization, Nontronite, PPHA, *Shewanella putrefaciens*

INTRODUCTION

Humic substances (HS) are an important component of organic matter in soils and sediments, which are often referred to as stable soil organic matter (Perdue et al., 1990). Studies have focused on adsorption behaviors of humic substances onto iron (oxyhydr) oxides and clay minerals (Chen et al., 2014; Coward et al., 2018; Coward et al., 2019; Eusterhues et al., 2008; Gouré-Doubi et al., 2018; Ha et al., 2008; Henneberry et al., 2012; Lv et al., 2016; Saidy et al., 2012; Sowers et al., 2019a; Theng, 1976; Vermeer et al., 1998; Zhang et al., 2012). In the 1990s, humic substances were demonstrated to shuttle electrons between microorganisms and Fe(III) oxide (Lovley et al., 1996). Since then, the role of HS as electron shuttle has been widely recognized in solid-phase Fe(III) reduction by microorganisms (Amstaetter et al., 2012; Fredrickson et al., 2000; Kappler et al., 2004; Liu et al., 2016; Lovley et al., 1998; Lovley et al., 1999; Shimizu et al., 2013). In these studies, organic compounds such as acetate and lactate typically serve as electron donors.

Although the electron shuttling role of natural HS is well established, it is still poorly understood whether they can serve as electron donor to reduce solid-phase Fe(III). Microbially reduced HS were able to reduce insoluble Fe oxides (Jiang and Kappler, 2008). Other studies showed that even native HS (nonreduced) could reduce aqueous Fe^{3+} (Peretyazhko and Sposito, 2006) and Fe(III) (oxyhr)oxides (Bauer and Kappler, 2009; Piepenbrock et al., 2014; Sundman et al., 2017), suggesting that native HS retain certain reduced functional groups under the ambient oxic condition. More recently, Stern et al. (2018) and Mejia et al. (2018) demonstrated that natural HS can play dual roles as electron donor and shuttle when coupled with bioreduction of ferrihydrite and hematite.

The ability of native HS to reduce Fe oxides is related to their intrinsic electron donating capacity (EDC) (Aeschbacher et al., 2012; Klüpfel et al., 2014). In these processes, humic substances may undergo some changes in functional groups (Aeschbacher et al., 2012) and composition (Mejia et al., 2018).

Fe-bearing clay minerals are common in soils and sediments, and structural Fe(III) in clays can be reduced either microbially or chemically (Dong et al., 2009; Pentráková et al., 2013; Stucki and Kostka, 2006). Despite common co-presence of clay minerals, HS, and microbes (Barré et al., 2014; Borden et al., 2010), the role of HS in clay redox reactions has not been well-studied. Most studies have used HS analog, anthraquinone-2,6-disulfonate (AQDS), as electron shuttle to enhance bioreduction of structural Fe(III) in clay minerals (Dong et al., 2009). To date, only a few studies (Liu et al., 2016; Liu et al., 2017; Lovley et al., 1998) have used natural HS as electron shuttle to enhance Fe(III) bioreduction in clays. However, it is currently unknown if natural HS can donate electrons to structural Fe(III) in clay minerals. Because clay minerals are fundamentally different from Fe oxides, in terms of both chemistry and structure, HS are expected to have different effects on electron transfer and mineral transformation. For example, reductive dissolution is a common consequence of Fe(III) oxide reduction (Weber et al., 2006), but clay minerals can undergo multiple redox cycles without much dissolution (Yang et al., 2012; Zhao et al., 2015). In this case, electron donation from HS to structural Fe(III) in clay minerals may be more difficult than Fe(III) (oxyhydr)oxides and may be directional (i.e., parallel to or perpendicular to the clay layers). It is not known how the EDC of HS affects their roles in electron donation and shuttling in clay bioreduction. Furthermore, the metal complexation properties of HS may differentially

affect clay mineral and (oxyhydr)oxide transformations. In addition, it remains unclear if HS undergoes any electrochemical and molecular change as a result of electron donation.

The objective of this study was to determine the role of natural HS as electron donor when coupled with reduction of structural Fe(III) in an iron-rich smectite, nontronite (NAu-2), in the absence and presence of an iron-reducing bacterium, *Shewanella putrefaciens* CN32. Specifically, the goals of the study were to determine: (1) the roles of HS as electron donor/shuttle in affecting abiotic and biotic Fe(III) reduction in nontronite; (2) the relationship between such roles and the physical/chemical properties of HS (EDC, molecular composition, metal ion complexation); (3) mineralogical transformation as a result of clay-HS-microbe interactions. We hypothesize that the EDC of natural HS determines the rate and extent of Fe(III) bioreduction, but the metal ion complexation of HS controls their role in mineral transformation. Furthermore, HS can undergo compositional change as a result of redox reactions. Wet chemical methods were used to monitor Fe(III) reduction. Electrochemistry, spectroscopy, microscopy, and mass spectrometry methods were employed to characterize changes of HS composition and mineralogy. The results of this study provide important insights into coupled Fe-C biogeochemical transformations in the environment.

MATERIALS AND METHODS

Materials and experimental setup

Nontronite (NAu-2), an Fe-rich smectite, was purchased from the Source Clays Repository of the Clay Minerals Society. It was originally collected from Uley Mine in

Southern Australia. The formula of this NAu-2 is $(Ca,Na,K)_{0.72}(Si_{7.55}Al_{0.45})(Fe_{3.83}Mg_{0.05})O_{20}(OH)_4$ (Keeling et al., 2000). Total Fe content of NAu-2 is 23.4%, with 0.6% as Fe(II) (Jaisi et al., 2005), while Mg content is about 0.15% (Gates et al., 2002). Fe(III) is distributed in both octahedral (92%) and tetrahedral sites (8%) (Gates et al., 2017; Jaisi et al., 2005). The NAu-2 sample was Na-saturated and size-separated as previously described (Jaisi et al., 2005). The size fraction of 0.02-0.5 μm was collected, dried, and made into 5 g/L suspension in 30 mM sodium bicarbonate buffer (29.76 mM $NaHCO_3$ and 1.34 mM KCl, pH 7.0), followed by purging (N_2:CO_2 80:20) and autoclaving.

Humic substances Leonardite humic acid (LHA, 1S104H) and Pahokee Peat humic acid (PPHA, 1S103H) were purchased from the International Humic Substances Society (IHSS) (Klüpfel et al., 2014; Rosario-Ortiz, 2015). These substances are natural organic matter obtained by alkali extraction, and the names do not imply secondary synthesis or chemical recalcitrance (Kleber and Lehmann, 2019; Lehmann and Kleber, 2015). According to the IHSS website, the carbon content of LHA and PPHA is 63.81% and 56.37%, respectively. Stock solutions (20 g/L) of LHA and PPHA were prepared by dissolving them in sodium bicarbonate buffer, followed by purging (N_2:CO_2 80:20) and filter sterilization (0.22 μm).

CN32 was originally purified from a subsurface rock at Cerro Negro in New Mexico and is routinely maintained in -80°C freezer. For this study, CN32 cells were cultured in a tryptic soy broth (TSB) (BD Bacto, Franklin Lakes, NJ) medium to the exponential growth phase.

Nontronite and humic acid stock solutions were suspended in bicarbonate buffer and

147 mixed in 30-mL serum bottles (suspension volume 8 mL) to achieve HS and NAu-2
148 concentrations of 2.5 g/L and 4.38 g/L [~18 mM Fe(III) conc.], respectively, with
149 *Shewanella putrefacien*s CN32 as a mediator. Although natural concentrations of HS
150 range from 0.1 to a few hundreds of mg C/L (Aiken et al., 1985), high concentrations of
151 LHA and PPHA were used here to facilitate observation of their effects on Fe(III)
152 reduction, similar to previous studies (Lovley et al., 1998; Lovley et al., 1996). CN32
153 cells of the exponential growth phase were washed by repeated centrifugation (at 2000 g
154 for 10 mins) and resuspension in anoxic and sterile bicarbonate buffer, and injected into
155 the experimental bottles to achieve $1x10^8$ cells/mL. For heat-killed microbial control,
156 autoclaved (121 ℃, 1 hour) cells replaced live ones. All experimental treatments were
157 performed in duplicate. The pH was checked to be 6.92-6.94 throughout the duration of
158 the experiments.

159 In order to study the effects of HS concentration and medium type on Fe(III)
160 reduction, another experiment was set up, in which two concentrations of HS (2.5 g/L
161 and 0.25 g/L) but the same NAu-2 concentration (4.38 g/L) were used in a growth
162 medium. The growth medium contained NH_4Cl (4.67 mM), KH_2PO_4 (4.41 mM), KCl
163 (1.34 mM), $NaHCO_3$ (29.76 mM), Wolfe's mineral solution (10 ml/L) and Wolfe's
164 vitamin solution (10 ml/L). The composition of Wolfe's mineral solution includes
165 nitrilotracetic acid (1.5 g), $MgSO_4 \cdot 7H_2O$ (3.0 g), $MnSO_4 \cdot H_2O$ (0.5 g), NaCl (1.0 g),
166 $FeSO_4 \cdot 7H_2O$ (0.1 g), $CoCl_2 \cdot 6H_2O$ (0.1 g), $CaCl_2$ (0.1 g), $ZnSO_4 \cdot 7H_2O$ (0.1 g),
167 $CuSO_4 \cdot 5H_2O$ (0.01 g), $AlK(SO_4)_2 \cdot 12H_2O$ (0.01 g), H_3BO_3 (0.01 g), and $Na_2MoO_4 \cdot 2H_2O$
168 (0.01 g) in 1.0 L distilled water. Wolfe's vitamin solution contains biotin (2.0 mg), folic
169 acid (2.0 mg), pyridoxine hydrochloride (10.0 mg), thiamine·HCl (5.0 mg), riboflavin

(5.0 mg), nicotinic acid (5.0 mg), calcium D-(+)-pantothenate (5.0 mg), vitamin B12 (0.1 mg), p-aminobenzoic acid (5.0 mg) and thioctic acid (5.0 mg) in 1.0 L distilled water. Cells were washed by repeated centrifugation (at 2000 g for 10 mins) and resuspension in the growth medium, and injected into the experimental bottles to achieve $1x10^8$ cells/mL. Because both CN32 cells (using energy reserves) (Jiang and Kappler, 2008; Klüpfel et al., 2014) and HS may be able to reduce Fe(III) in NAu-2, it is important to determine their electron donating capacities so that electron balance may be calculated. If CN32 cells could donate electrons, they might transfer electrons to HS first and reduced HS then donate electrons to Fe(III). Therefore, in a supplementary experiment, CN32 cells ($1x10^8$ cells/mL) were mixed with HS in the growth medium (2.5 g/L or 0.25 g/L) for two days to allow reduction of HS by CN32 cells. After removal of CN32 cells by filtration, NAu-2 (4.38 g/L) was added to reduced HS. By comparing the amount of Fe(II) produced by reduced and nonreduced HS, the amount of Fe(III) reduction that was contributed by CN32 cells was calculated.

Analytical methods

Time course production of total Fe(II) was measured to monitor the progress of Fe(III) reduction. Electron donating capacity (EDC) was measured for aqueous HS before and after Fe(III) bioreduction under growth condition (Table 1), because more changes were expected in this experiment. Fourier-transform ion cyclotron resonance mass spectrometry (FT-ICR-MS) was used to measure chemical changes of HS from both the buffer and growth medium experiments. Preliminary analyses revealed similar changes in solid phase between the two types of experiments. Therefore, all solid analyses were

performed for the bicarbonate buffer bioreduction experiment under non-growth condition only (for the HS concentration of 2.5 g/L). Fourier-transform infrared spectroscopy (FTIR) and Time-of-flight secondary ion mass spectrometry (ToF-SIMS) were used to determine the changes of chemical/molecular compositions of HS. X-ray diffraction (XRD), Scanning electron microscopy (SEM) and Transmission electron microscopy (TEM) were used to observe mineralogical transformations after Fe(III) reduction.

Total Fe(II) and Fe(III) measurements. Production of Fe(II) over time was measured with the 1,10-phenanthroline method (Amonette and Templeton, 1998). The only modification was that after addition of 5% H_3BO_3 clay suspension was centrifuged at 12,000 g for 20 minutes to remove precipitated humic acids before absorbance measurement at 510 nm. Specifically, 0.2 mL clay suspension was first added to 0.48 mL H_2SO_4 (3.6 N). Hydrofluoric acid was then added to dissolve the clay suspension. 1,10-phenanthroline assay measures total Fe(II) (Boyanov et al.). To measure total Fe, Fe(III) was first reduced to Fe(II) with hydroxylammonium chloride (Sigma) and then total Fe(II) was measured with the 1,10-phenanthroline assay. A negligible amount of Fe(II) in those experiments without NAu-2 might be sourced from the HS (Zaccone et al., 2007b).

Measurement of electron donating capacity (EDC). Clay-HS samples were centrifuged at 12,000 g for 30 mins to remove CN32 cells and NAu-2. The EDC values of aqueous HS samples were measured using a mediated electrochemical oxidation

(MEO) method developed previously (Aeschbacher et al., 2010; Klüpfel et al., 2014). The measurements were performed on an electrochemical workstation (PGSTAT302N, Metrohm, Switzerland) inside an anaerobic chamber at room temperature. The electrochemical cell was filled with 80 mL PIPES buffer (10 mM) which was pre-purged with N_2 to remove oxygen. The Eh of the buffer solution was set at +0.7 V. After the current was stabilized, 100 μL stock solution (10 μM) of electron transfer mediator zwitterionic viologen 4,4′-bipyridinium-1,1′-bis(2-ethylsulfonate) (ZiV) was added to the cell with a micro-syringe. After the oxidative current peak became stabilized, a certain amount (200–750 μL) of aqueous sample was added to the cell with a micro-syringe. The MEO current peaks were monitored and integrated to yield the EDC of the samples. All samples were analyzed in triplicates.

Fourier-transform ion cyclotron resonance mass spectrometry (FT-ICR-MS). Clay-HS samples were centrifuged at 12,000 g for 30 mins. Supernatants were solid phase extracted (SPE) and eluted with methanol based on a previous study (Dittmar et al., 2008). Specifically, the supernatant samples were diluted to 5 mL total volume with nanopore/MilliQ (18Ω) H_2O and acidified to pH 2 with 85% H_3PO_4 (~ 2 μL of 85% H_3PO_4 for 5 mL sample). Samples were loaded onto a cartridge after activation with 1mL of methanol. Samples were allowed to elute through a column with a Bond Elut-PPL solid phase extraction cartridge (Agilent, USA). Eluants were injected into a 12 Tesla Fourier transform ion cyclotron resonance mass spectrometer (12T FTICR MS) (Bruker SolariX). Negatively charged primary molecular ions were generated with a standard Bruker electron spray ionization (ESI) source. Samples were introduced to the

primary ions through a syringe pump at a flow rate of 3.0 μL/min. Experimental parameters were set as follows: 3.5 kV spray shield voltage, 4.0 kV capillary voltage, and -320 V capillary column end voltage. Each sample was co-added with 144 scans and internally calibrated using $–CH_2$ groups. A *m/z* range of 100-800 was collected with a mass measurement accuracy of < 1 ppm. Chemical formulas were assigned using in-house software Formularity (Tolić et al., 2017) following the Compound Identification Algorithm described by Kujawinski and Behn (2006), and modified by Minor et al.,(2012) and further developed by Tolic et al.,(2017) with about 84% assignment for LHA group and 89% assignment for PPHA group.

Statistical analysis was performed to assign molecular formulas for each sample based on the number of carbon (C#), hydrogen (H#), oxygen (O#), nitrogen (N#), and phosphorus (P#). The magnitude-weighted parameters, including DBE (double bond equivalent), DBE/O, DBE-O, and AI (aromatic index), were calculated. DBE represents the degree of unsaturation and DBE/O ratios are inversely related to the possible number of C=O bonds (i.e., DBE per O)(Roth et al., 2013). Moreover, DBE-O is used to describe C=C unsaturation by omitting all possible C=O bonds. AI is used to describe the aromaticity of a compound. All magnitude-weighted parameters were calculated as the sum of all compounds of chemical information and relative intensity by the following formulas (Koch and Dittmar, 2006; Sleighter and Hatcher, 2008; Sleighter et al., 2010):

$$DBE=1/2*(2C+N+P-H+2)$$

$$(DBE)_w=\sum(DBE_n*M_n)$$

$$(DBE/O)_w=\sum[(DBE/O)_n*M_n]$$

$(DBE\text{-}O)_w=\sum[(DBE\text{-}O)_n*M_n]$

$AI=\sum[\ (1+C\text{-}O\text{-}S\text{-}0.5H)/(C\text{-}O\text{-}S\text{-}N\text{-}P)]n*\ M_n]$

Where *w* signifies a magnitude-weighted calculation, *n* signifies that the parameter is calculated for every assigned molecular formula, # represents the number of the specified atoms in the molecular formula, and M_n is the relative intensity of each formula.

Fourier-transform infrared spectroscopy (FTIR). FTIR was used to study structural changes of HS and NAu-2 after reduction. Clay-HS suspension was dried on a parafilm in an anaerobic chamber for 2 days to form a thin and flat pellet. After drying, the clay pellet was carefully removed from the parafilm. Pure NAu-2 and HS controls were measured in powder. Attenuated total internal reflection (ATR) infrared spectra were collected using a Perkin Elmer Spectrum One FTIR that is interfaced to a Harrick Split-Pea ATR accessory. A Ge internal reflection element (IRE) was used and a loading of 0.5 kg pressure was applied to the sample to achieve a good contact. FTIR spectra were collected at a 4 cm^{-1} resolution over a range of 4000-400 cm^{-1}. Each spectrum represented the average of 32 individual scans. Before every scan, a background air spectrum was taken, and subtracted from sample spectra automatically by the control software.

Time-of-flight secondary ion mass spectrometry (ToF-SIMS). ToF-SIMS was employed to determine any chemical changes on solid surface as a result of oxidation of HS when coupled with reduction of Fe(III) in NAu-2. Clay suspensions were

centrifuged and pellets were dried in an anaerobic chamber. Pellet samples were analyzed on a ToF-SIMS instrument with a bismuth liquid metal ion gun at 25 KeV. Bi^{3+} was chosen as the primary ion by using appropriate mass filter settings. The pulse width of the primary ion was <1.0 ns. The target current was ~0.58 pA with a scanning area of 200 μm × 200 μm. ToF-SIMS spectra were obtained in both negative (extraction voltage +2.0 kV) and positive secondary ion modes (extraction voltage -2.0 kV) with three spot analyses per sample. The results were internally calibrated (negative with H^-, F^-, and CN^-, and positive with H^+, CH^+, and Fe^+) followed by principal component analysis (PCA) in Matlab (Ding et al., 2016; Hua et al., 2016). PCA is a statistical method used to find combinations of variables that characterizes the most important trends in the data. PCA of ToF-SIMS data helps to find out the relations between molecular species contained in complex systems. Peaks in the mass range of *m/z* 0-400 acquired in negative mode were selected to perform PCA. All peaks were normalized to total ion signal intensity.

X-ray diffraction (XRD). XRD was performed to study mineral phase changes after reduction. XRD samples were prepared by mounting clay suspension on a petrographic slide and dried in an anaerobic chamber (98% N_2, 2% H_2, Coy Laboratory Products, Grass Lake, Michigan). To differentiate expandable clays (nontronite NAu-2) from non-expandable clays, such as illite, XRD patterns were also obtained by placing dried samples overnight in an ethylene glycol desiccator to allow expansion of nontronite interlayers. To minimize air oxidation, samples were sealed with vacuum glue during XRD analysis. XRD patterns were collected using a Scintag X1 X-ray diffractometer

with CuKa radiation, a fixed slit scintillation detector, and power of 1400 W (voltage, 40 kV, current, 35 mA). Scans were collected over a range of 2-35°(2θ) with a step size of 0.01° and dwell time of 10 s per step. Mineral phases were identified using MDI Jade 7 software (Zhao et al., 2013).

Scanning electron microscope (SEM) observation. SEM observations were made to observe cell-mineral associations, and any mineralogical changes as a result of Fe(III) reduction. A small amount of clay suspension (0.2 mL in volume) was withdrawn from the experimental bottles inside an anaerobic chamber with a sterile syringe needle and mounted onto a glass cover slip. To promote adhesion of particles to the substrate the glass cover slip was pretreated with 0.1% poly-l-lysine for 1 hour at room temperature. Multiple cover slips were stacked into a sample holder (vertically separated by wavy washers) and submerged in a fixative solution (2% paraformaldehyde and 2.5% glutaraldehyde in 0.05 M sodium cacodylate, pH 7.2) for 30 minutes, followed by rinsing with the same buffer twice and ddH_2O twice. A series of dehydration steps was carried out followed by CO_2 critical point drying with a Tousimis Samdri-780A Critical Point Dryer (CPD) (Dong et al., 2003). All cover slips were attached onto SEM aluminum stubs with double-sided sticky tape and gold-coated for 45 seconds (~10 nm coating) with a Denton Desk II sputter coater. The prepared samples were observed with a Zeiss Supra 35 SEM, which was equipped with a Bruker Energy Dispersive Spectroscopy (EDS) detector. The SEM was operated using 10 KeV accelerating voltage and 8.5 mm working distance. EDS spectra were collected for 5 minutes to determine the chemical composition of various minerals. To obtain representative images, several

tens of images were collected from 3-5 cover slips.

Transmission electron microscope (TEM) observation. To further observe mineralogical changes at a high spatial resolution, reduced samples were observed under TEM. Clay suspensions were washed with anoxic and sterilized bicarbonate buffer (pH 7.0) and diluted by a factor of 30. Diluted suspensions were pipetted onto 300 mesh copper grids, which were covered with carbon-coated nitrocellulose membrane support film. All samples were dried overnight in an anaerobic chamber. TEM observations and analyses were carried out on a JEOL JEM-2100 LaB_6 TEM-STEM at a 200 KeV accelerating voltage. Bright-field TEM images and selected area electron diffraction patterns (SAED) were captured with a Gatan Orius SC200D camera and processed with the Digital Micrograph software. EDS spectra were collected for 5 minutes with a Bruker AXS Microanalysis Quantax 200 with 4030 SDD detector. To obtain representative images, several tens of images were collected from 3-5 grids.

RESULTS

Reduction of Fe(III) in NAu-2 with HS as electron donor

In the presence of HS, CN32 reduced structural Fe(III) in nontronite under both non-growth (i.e., bicarbonate buffer, Fig. 1) and growth conditions (Fig. 2A&B). In bicarbonate buffer, a substantial amount of Fe(II) was measured at time zero with 2.5 g/L LHA and PPHA (Fig. 1), suggesting rapid abiotic reduction of Fe(III). The amount of Fe(II) produced only slightly increased over time. In the presence of CN32 cells, both the rate and extent significantly increased. Between the two HS, PPHA reduced more Fe(III) at a higher rate. The final bioreduction extent was 12.2% and 17.8% with LHA

and PPHA, respectively.

In growth medium with a 2.5 g/L HS concentration, redox reactions also occurred among HS, CN32 cells, and NAu-2 (Fig. 2A&2B). Both HS and CN32 cells were able to reduce Fe(III) in NAu-2. In the LHA + NAu-2 treatment, the amount of Fe(II) produced [~0.4 mmol Fe(II) produced per g LHA, Fig. 2A] was similar to that in bicarbonate buffer over the same time frame (8 days), but higher than the corresponding amount of EDC decrease (0.12 mmol e^-/g LHA, Fig. 2E). Unexpectedly, CN32 cells also reduced a substantial amount of Fe(III) (Fig. 2A). There was also a redox reaction between CN32 and LHA, which was determined by a supplementary experiment. CN32-reduced LHA reduced more Fe(III) than nonreduced LHA (Fig. 2C). In this case, the net amount of Fe(II) increase i.e., ~ 0.4 mmol Fe(II) per g of LHA, was similar to the amount of corresponding amount of EDC increase (i.e., 0.5 mmol e^-/g, Fig. 2E). This result suggests that the electrons transferred from CN32 cells to LHA were subsequently used to reduce structural Fe(III) in NAu-2, therefore LHA did not retain any of the CN32-derived electrons. The total extent of Fe(III) reduction in the ternary treatment (CN32 + LHA + NAu-2, 5.6 mM) was higher than the sum of those in the two binary treatments, i.e., in CN32 + NAu-2 treatment (4 mM) and in LHA + NAu-2 treatment (1.1 mM), suggesting that addition of CN32 cells made more LHA available to reduce Fe(III). The amount of Fe(III) reduction contributed by LHA (1.6/2.5 = 0.6 mmol e-/g LHA) was again higher than the corresponding amount of EDC decrease (i.e., 0.2 mmol e^-/g LHA).

Relative to LHA, PPHA exhibited a higher reducing capacity than LHA (Fig. 2B), apparently because of its higher EDC value (Fig. 2E). In the PPHA+NAu-2 treatment,

the amount of Fe(II) produced (1.1 mmol Fe(II) produced per g PPHA) was higher than the corresponding amount of EDC decrease (0.42 mmol/g PPHA, Fig. 2E). Again pre-reduced PPHA by CN32 reduced more Fe(III) than nonreduced PPHA (Fig. 2D). The net amount of Fe(II) increase by pre-reduced PPHA relative to pristine PPHA, i.e., ~ 0.4 mmol Fe(II) per g of PPHA, was the same as the corresponding amount of EDC increase (i.e., 0.4 mmol/g, Fig. 2E). The extent of Fe(III) bioreduction in the ternary CN32 + PPHA + NAu-2 treatment (7.1 mM) was slightly higher than the sum of those in the two binary treatments, i.e., in CN32 + NAu-2 treatment (4.0 mM) and in PPHA + NAu-2 treatment (2.8 mM), suggesting that addition of CN32 cells made more PPHA available to reduce Fe(III), similar to the LHA experiment. The amount of Fe(III) reduction contributed by PPHA (1.2 mmol/g PPHA) was higher than the amount of EDC decrease (i.e., 0.7 mmol/g PPHA).

When the concentrations of LHA and PPHA decreased to 0.25 g/L, abiotic reduction of Fe(III) by these HS was negligible (Fig. 2A&2B). Interestingly, the extent of Fe(III) reduction in the ternary treatment (NAu-2+HS+CN32 cells) was higher than the sum of those from the two binary systems (NAu-2 + HS and NAu-2 + CN32 cells). For example, for both LHA and PPHA, the extent of Fe(III) reduction was ~5 mM, but the sum of those from the two binary treatments was only ~4 mM. This result suggests that more LHA and PPHA became available to reduce Fe(III) due to addition of CN32 cells. The amounts of CN32-enabled LHA and PPHA reduction capacities at 0.25 g/L (~1 mM) were higher than those at 2.5 g/L (~0.3 mM), suggesting that CN32 cells were able to use more LHA and PPHA when electron donor/carbon sources were limited. Because of limited electron accepting capacities (EAC) of HS at 0.25 g/L, there was little difference

in the rate and extent of Fe(III) reduction by pre-reduced and nonreduced HS (Fig. 2C&2D).

Reduction-induced structural changes of LHA and PPHA revealed by FTIR

In the range of 1800-1100 cm^{-1} (Fig. 3), the aromatic C=C stretching band of LHA and PPHA (1609 cm^{-1} and 1617 cm^{-1}, respectively) (Reza et al., 2012) shifted to 1623 and 1633 cm^{-1} (Fig. 3), respectively, after reaction with NAu-2. After reaction with both NAu-2 and CN32 cells, the intensities of these peaks decreased. Moreover, the C-O stretching motions in the phenol moiety of both PPHA and LHA (Sánchez-Cortés et al., 1998) (at 1214-1219 cm^{-1}) disappeared after Fe(III) reduction regardless of the absence or presence of CN32 cells, suggesting the involvement of the phenolic group of these HS in Fe(III) reduction.

Reduction-induced compositional changes of aqueous HS revealed by FT-ICR-MS

The van Krevelen diagrams for the samples in bicarbonate buffer showed little change after reaction with NAu-2 (Figure S1). However, the magnitude-weighted parameters, which have been successfully used in the studies of organic matter composition (Flerus et al., 2011; Koch et al., 2005; Roth et al., 2013), showed important changes. The overall changes of these parameters were more apparent for treatments in growth medium (Table 2) than in bicarbonate buffer (Table S1) and in the presence of PPHA than in the presence of LHA. (Tables 1 and S1). These results were consistent with the higher extents of Fe(III) reduction under growth condition and in the presence of PPHA (Fig. 2B). Interestingly, the DBE, DBE/O, DBE-O, and AI (aromatic index) parameters

423 of both LHA and PPHA did not change from control to abiotically oxidized products but
424 decreased upon addition of CN32 cells (by 1-15%). Previous studies have shown that
425 changes in a few percent (2-13%) are considered significant (Roth et al., 2013; Seifert et
426 al., 2016; Waggoner and Hatcher, 2017). The DBE-O is used to describe C=C
427 unsaturation by omitting all possible C=O bonds that are abundant in RCOOH
428 functional group (D'Andrilli et al., 2010). The decrease in the DBE-O value with
429 addition of CN32 indicates partial oxidation of LHA and PPHA that involve aromatic
430 compounds (D'Andrilli et al., 2010). The decreased AI value suggests a compositional
431 change from unsaturated aromatic compounds to saturated compounds, consistent with
432 photochemically induced degradation of dissolved organic matter (Gonsior et al., 2009).
433 Consistent with the EDCs and Fe(III) reduction extents (Figs. 1 & 2), these changes
434 were more dramatic for PPHA than for LHA (Table 2).
435
436 **Reduction-induced molecular changes of LHA and PPHA revealed by ToF-SIMS**
437 As a complementary technique to FT-ICR-MS, ToF-SIMS is capable of detecting
438 reduction-induced changes of chemical and molecular composition of sorbed HS and the
439 underlying NAu-2. Relative to HS and NAu-2 mixtures, addition of heat-killed cells
440 decreased PC2 scores (Fig. 4). The positive loadings of PC2 are mainly F-related
441 clusters such as F^-, F_2^-, CF_3^-, and the negative loadings of PC2 are mainly N-rich organic
442 clusters (Fig. 4C). A decrease of PC2 scores suggests that addition of dead cells
443 increased microbially-derived organic species. Live cell addition resulted in higher
444 scores of PC1 (Fig. 4A). The positive loadings of PC1 are mostly N-rich organic species
445 and PO_x. The negative loadings are SiO_x and hydro-carbon (from humic acids) related

446 species (Fig. 4B). A positive PC1 shift indicates more microbially-derived molecular
447 clusters and less HS-derived clusters, suggesting that microbial Fe(III) reduction
448 produced organic materials of microbial origin at the expense of HS. An increased score
449 of PC1 also indicates less detection of mineral surface (Si-O surface), suggesting that
450 more mineral surface might be covered by microbially-derived organic species.
451
452 **Reduction-induced mineralogical changes**
453 Although LHA reduced a lower amount of Fe(III) than PPHA (Figs. 1&2), its effect
454 on mineral transformation was more substantial (Fig. 5). After one-month incubation,
455 while the NAu-2 control showed nontronite peaks only with no impurity minerals (Fig.
456 5A), consistent with the result of the Keeling et al. (2000) on the same size fraction
457 (<0.5 μm), several new peaks emerged in reduced samples in the presence of LHA
458 (denoted with arrows in Fig. 5A). These new peaks emerged in the presence of LHA
459 alone but became more intense after addition of live CN32 cells. A prolonged incubation
460 time, along with a comparison between XRD patterns of air-dried and ethylene
461 glycolated samples allowed positive identification of these new peaks (Fig. 5B). The
462 peak at 2-theta of 24° in the one-month sample (Fig. 5A), possibly a type of zeolite,
463 disappeared after prolonged incubation (Fig. 5B), suggesting its transient nature. Two
464 small peaks at 2-theta of 9.45 and 28.59°, which remained after 9-month incubation,
465 matched the two strongest lines of standard talc [d(001) and d(003), Joint Committee on
466 Powder Diffraction Standards (JCPDS) # 19-0770, also see (Gunter et al., 2016; Kursun
467 and Ulusoy, 2006), among others]. A previous study similarly observed these two
468 strongest lines of talc (Liu et al., 2016). One peak at 2-theta of 28°, which remained after

prolonged incubation (Fig. 5B), matched the strongest line [d(002)] of disordered albite [JCPDS #10-0393, also see (Xu et al., 2017)]. Because the strongest peak was small, other weaker peaks were not visible [see for example Fig. 5A in (Hupp and Donovan, 2018)]. As expected, ethylene glycolation shifted all nontronite peaks to smaller 2-theta (larger d spacings), but the talc and albite peaks remained at the same positions. Secondary minerals in the presence of both LHA and CN32 cells (data not shown) were similar to those with the presence of LHA only. In contrast to LHA, no new peaks emerged after one-month incubation in the presence of PPHA (Fig. 5C).

SEM observations confirmed XRD data showing the formation of these new minerals in LHA-treated samples(Fig. 6). The original NAu-2 particles exhibited a flaky and wavy shape (Fig. 6A) with a typical nontronite composition but with a small Fe peak. A small Fe peak has been observed in multiple studies of NAu-2 (for example, Liu et al., 2016; Zhao et al., 2013). Absorption of characteristic X-ray of Fe by sample itself or Au coating could be a possible reason. After reduction, NAu-2 particles gained some K and Al, and lost Fe, yielding a composition similar to high-charge smectite or mixed-layer illite-smectite (Fig. 6B). Sapodilla-like silica oxide also formed (Fig. 6C), likely in an amorphous form, because quartz was not detected in XRD pattern (Fig. 5). Unexpectedly, ilmenite ($FeTiO_3$) was observed in the reduced sample, with 1.2 x 3 μm in size (black arrow in Fig. 6C), in the same field of view as CN32 cells (white oval in Fig. 6C). The corresponding EDS spectrum showed O, Fe, and Ti, and Si. The Si peak was always present, , apparently due to abundant silica available from reductive dissolution of NAu-2 (see silica oxide in Fig. 6C). Furthermore, albite [$NaAlSi_3O_8$] was observed (white arrow in Fig. 6D and black arrow Fig. 6E). Talc [$Mg_3Si_4O_{10}(OH)_2$] was

found in the same field of view as albite (white arrow Fig. 6E). Talc with a layered structure was also observed (Fig. 6F). A small amount of Fe was observed in talc, possibly forming a Mg-Fe solid solution (Agangi et al., 2018; Forbes, 1969; Howe, 2017). Al peak was absent in fibrous talc but present in layered talc. The common presence of albite and talc under SEM was consistent with XRD data (Fig. 5).

TEM observations of the reduced NAu-2-LHA sample confirmed XRD and SEM results. A talc particle of ~1.8 x 2.4 μm in size was observed under TEM (Fig. 7A). An enlarged TEM image showed subtle lattice fringes (Fig. 7B). The corresponding SAED pattern showed a pseudo-hexagonal electron diffraction pattern (Fig. 7C). The ideal composition of talc is $Mg_3Si_4O_{10}(OH)_2$, but the Fe content was quite high, apparently due to abundant Fe available from reductive dissolution of NAu-2. Fe can substitute Mg in trioctahedral sites in the talc structure to form a Mg-Fe solid solution (Forbes, 1969). Ilmenite particles were also commonly observed with a typical size of ~1.4 x 1.2 μm (Fig. 8A). A high-resolution TEM image of ilmenite displayed 0.27 nm and 0.25 nm lattice fringes (Fig. 8B), corresponding to reflections of (1 0 4) and (-1 2 0), respectively. Even in thin edges of ilmenite, the corresponding EDS spectrum always contained a certain amount of Si (Fig. 8C). Under high resolution, there appeared to be another phase that was intimately mixed with ilmenite (Fig. 8D). To separate the two phases, a series of SAED patterns were obtained by slowing moving the sample stage. In doing so, SAED patterns for pure ilmenite and ferrihydrite were obtained (Fig. 8D-F). Based on these end members, the mixed SAED pattern was deconvolved into three sets: 1) one ferrihydrite crystal, taken along the [0 $\overline{2}$ 0] zone axis, based on Michel et al.(2007) (Fig. 8D); 2) a polycrystalline ferrihydrite (concentric rings) with d-spacings of 0.45,

515 0.26, 0.17, 0.15, and 0.13 nm (Fig. 8E); 3) an ilmenite single crystal pattern taken along
516 the [4 2 $\overline{1}$] zone axis (Fig. 8F). As expected, the SAED pattern of ilmenite displayed
517 reflections (1 0 4) and ($\overline{1}$ 2 0), consistent with the lattice fringe images (Fig. 8B).
518
519 **DISCUSSION**
520 **HS as electron donor to reduce structural Fe(III) in nontronite**
521 A few studies have investigated abiotic reduction of solid-phase Fe(III) by HS. While
522 an early study did not show reduction of poorly-crystalline Fe(III) oxides by natural
523 (nonreduced) HS (Lovley et al., 1996), subsequent studies showed some abiotic
524 reduction of aqueous Fe^{3+} (Peretyazhko and Sposito, 2006) and solid-phase Fe(III) by
525 nonreduced LHA and/or PPHA (Bauer and Kappler, 2009; Piepenbrock et al., 2014;
526 Sundman et al., 2017). When a high concentration of LHA (2 g/L) was used, aqueous
527 Fe^{3+} was reduced by nonreduced LHA (Peretyazhko and Sposito, 2006). At a low HS
528 concentration (~0.3 g/L), nonreduced PPHA reduced small amounts of poorly crystalline
529 ferrihydrite (Bauer and Kappler, 2009; Piepenbrock et al., 2014). At 0.6 g/L, PPHA also
530 reduced a negligible amount of Fe(III) in magnetite (Sundman et al., 2017). These
531 studies collectively illustrate that intrinsically reduced functional groups present in
532 native HS are able to reduce solid-phase Fe(III). However, the extent of reduction is
533 limited, likely because of low HS concentrations used in previous experiments.
534 Our study demonstrated that native LHA and PPHA significantly reduced structural
535 Fe(III) in nontronite. Compared to Fe(III) oxides (reduction extents of 0.13-1.3%)
536 (Bauer and Kappler, 2009; Piepenbrock et al., 2014; Sundman et al., 2017), this study
537 revealed much higher extents of Fe(III) reduction in nontronite NAu-2 (12.2 and 31.1%

for 2.5 g/L LHA in bicarbonate and growth medium, respectively; 17.8 and 39.0% for 2.5 g/L PPHA in bicarbonate and growth medium, respectively). These much higher extents were likely because of a higher concentration of HS used (2.5 g/L in this work versus 0.3-0.6 g/L in Fe-oxide studies). However, at a low concentration (0.25 g/L), abiotic reduction was negligible (Fig. 2A-B). Interestingly, when CN32 cells were present, LHA and PPHA donated more electrons to NAu-2. This result suggests that CN32 cells were able to make additional electrons of LHA and PPHA available to reduce more structural Fe(III) in NAu-2.

LHA and PPHA changes after electron donation to NAu-2

Although our measured EDCs of LHA and PPHA (0.86 and 0.95 mmol e- per gram C, respectively) fell within the previously reported ranges (1.9-2.4 and 1.0-1.8 mmol e- per gram C, respectively, Klüpfel et al., 2014; Zheng et al., 2019), the relative magnitude between LHA and PPHA was different. Nonetheless, our EDC data were consistent the Fe(III) reduction extent, i.e., PPHA with a higher EDC reduced more Fe(III) (Figs. 1&2A-B). These data suggest that different batches of humic acids from the IHSS, even under the same name, may have different EDC values and reduction capacities. The following discussion is focused on the relative change of EDC.

A comparison between the amount of Fe(III) reduction (Fig. 2A-B) and the amount of EDC changes (Fig. 2E) suggests that the amount of Fe(III) reduction was in general higher than the corresponding amount of EDC decrease, i.e., excess amounts of Fe(III) were reduced relative to the amount of EDC decreased. Because EDC was measured for aqueous LHA and PPHA, and it is known that LHA and PPHA can sorb onto clay

561 mineral surface (Ghosh et al., 2009; Liu et al., 2017; Wang and Xing, 2005; Zhang et al.,
562 2012), it is likely that aqueous HS may have only partially contributed to Fe(III)
563 reduction. Sorbed HS may be important in reducing structural Fe(III) as well. Indeed, a
564 previous study (Liu et al., 2017) observed significant amounts of Fe(III) reduction in
565 NAu-2 by sorbed HS. Because mineral-sorbed and aqueous HS generally have different
566 chemical composition and functional groups, due to sorptive fractionation of HS (Zhang
567 et al., 2012), they are expected to have different Fe(III) reduction capacity (Liu et al.,
568 2017; Sowers et al., 2019b). Sorbed HS may be more readily donating electrons to
569 structural Fe(III) in NAu-2, because of spatial proximity to the structural Fe(III).
570 Therefore, more decrease in EDC is expected for sorbed HS, which would account for
571 excess Fe(III) reduction relative to the measured EDC decrease of aqueous HS. Direct
572 EDC measurement of sorbed HS was not possible because of their association with
573 NAu-2.

574 Our FTIR, ToF-SIMS, and FT-ICR-MS data support this scenario in showing that
575 sorbed HS exhibited significant compositional change. For example, our FTIR data
576 revealed that, after LHA and PPHA donated electrons to Fe(III), their peaks at
577 1214-1219 cm^{-1} disappeared (Fig. 3), suggesting that the phenolic moieties of sorbed HS
578 were responsible for electron donation to Fe(III), consistent with a previous study
579 (Aeschbacher et al., 2012). Furthermore, the positions of the aromatic C=C stretching
580 bands of sorbed LHA and PPHA shifted after they donated electrons to Fe(III), but
581 addition of CN32 cells only decreased their intensity. These changes were consistent
582 with the reduction data, showing that most LHA and PPHA were oxidized abiotically by
583 NAu-2, and addition of CN32 only slightly oxidized some LHA and PPHA (Fig. 2A-B).

584 In comparison to sorbed HS, aqueous LHA and PPHA did not show much change
585 after abiotic reaction with NAu-2, but exhibited some change in the presence of CN32
586 cells (Table 2). These trends suggest that abiotic reduction of NAu-2 may have been
587 accomplished by sorbed HS, perhaps because of their spatial proximity to the Fe(III)
588 centers in the NAu-2 structure. Electron transfer from sorbed HS to structural Fe(III) in
589 NAu-2 should have occurred fast [i.e., nearly instantaneous Fe(II) production at time
590 zero, Figs. 1&2A-B]. In contrast, biotic reduction of NAu-2 may have been largely
591 achieved by aqueous HS. In this case, electron transfer from aqueous HS and cells
592 would have been slower (Figs. 1&2A-B, because of spatial distance and site blocking of
593 NAu-2 surface by sorbed HS, similar to the site blocking of Fe-oxides by sorbed HS
594 (Piepenbrock et al., 2011).

595 The observation that *S. putrefaciens* CN32 was able to use HS as electron donor was
596 unexpected, because this strain is known to only utilize simple compounds, such as
597 lactate and H_2 as electron donors when coupled with reduction of structural Fe(III) in
598 clay minerals (Dong et al., 2009; Zhao et al., 2013; Zhao et al., 2015). However, LHA
599 and PPHA are alkaline extracts of natural organic matter (Kleber and Lehmann, 2019;
600 Lehmann and Kleber, 2015) and likely contain bioavailable electron donors such as
601 amino acids (Sutton and Sposito, 2005). Indeed, previous studies (Cao and Jiang, 2019;
602 Yang et al., 2016) showed that low molecular weight fractions of LHA and PPHA
603 accounted for 0.4-2% of the total carbon content in these HS. Therefore, small
604 molecules of HS may have been utilized by CN32.

605

606 **_S. putrefaciens_ CN32 as electron donor to reduce structural Fe(III) and HS**

607 Our data demonstrated that this bacterium itself can serve as electron donor to reduce
608 Fe(III) and HS (Fig. 2A and 2B). A few studies have reported reducing capacity of
609 bacterial cells (Jiang and Kappler, 2008; Klüpfel et al., 2014; Mejia et al., 2018). In one
610 study (Jiang and Kappler, 2008), *Geobacter sulfurreducens* reduced HS without any
611 known electron donor. The authors concluded that either the cells stored electron
612 equivalents or HA contained some electron donors such as amino acids (Sutton and
613 Sposito, 2005). Similarly, Klüpfel et al. (2014) observed reduction of PPHA by *S.*
614 *oneidensis* and the authors ascribed this to electron donors present in either lactose
615 mother liquor medium (Achal et al., 2009) or intracellular biomass. Mejia et al. (2018)
616 observed ferrihydrite bioreduction by HS but without any known electron donor.
617 Likewise, our bicarbonate buffer and growth medium did not contain any electron donor
618 other than HS. Pre-reduced HS by CN32 cells reduced more Fe(III) relative to
619 un-reduced HS, and the amount of enhancement was the same between LHA and PPHA
620 (Fig. 2C and D). More importantly, CN32 cells reduced structural Fe(III) even without
621 any HS. Therefore, in this case, energy reserve or secreted substances of CN32 cells
622 more likely served as electron donors. Interestingly, this intracellular reducing capacity
623 has been reported for an Fe(II) oxidizer *Pseudogulbenkiania* sp. strain 2002 (Weber et
624 al., 2001; Zhao et al., 2013).
625
626 **Secondary mineralization**
627 Because of the presence of talc, ilmenite, and plagioclase in the > 2 μm size fraction
628 of nontronite NAu-2 (Keeling et al., 2000), some of these mineral phases observed could
629 have been inherited from the original NAu-2, despite the fact that the size fraction of

630 0.02-0.5 μm used in this study was free of any impurities (Keeling et al., 2000). Several
631 lines of evidence suggest that talc and albite are newly formed from reductive
632 dissolution of NAu-2 by HS and CN32 cells. First, the size same fraction of NAu-2
633 control (0.02-0.5 μm) did not show any of these impurities (Fig. 5A). Second, all XRD
634 patterns in PPHA treatments did not show any new mineral formation (Fig. 5C). Third,
635 time-course XRD data showed that talc and albite formed only at a later stage of
636 reduction (4 and 12 days, respectively, data not shown), not at the beginning. Fourth,
637 under both SEM and TEM talc and albite were commonly observed in reduced samples,
638 but were never observed in unreduced NAu-2 control. These HA- and time-dependent
639 formations of talc and albite suggest that they were newly formed, likely via a
640 dissolution-precipitation mechanism (Liu et al., 2015; Liu et al., 2016). Although
641 ilmenite was not present in the < 0.5 μm size fraction of the original NAu-2 either
642 (Keeling et al., 2000), its reduction-induced formation was less convincing, because it
643 was not detected by XRD in either unreduced or reduced samples (Fig. 5). SEM and
644 TEM observations were not sufficient to suggest their exact origin, because some
645 ilmenite particles in the original NAu-2 may have escaped size fractionation and made
646 into the < 0.5 μm size fraction. However, the ilmenite composition consistently showed
647 the presence of Si, likely because the aqueous solution was in excess of Si (as evidenced
648 by silica oxide precipitation, Fig. 6C). In addition, the intimate association of ilmenite
649 and ferrihydrite (Fig. 8) further suggests that ilmenite observed might not be entirely
650 from the original NAu-2, because ferrihydrite was absent in the original NAu-2 (Keeling
651 et al., 2000). In this case, a certain amount of Ti associated with HS (Zaccone et al.,
652 2007a) can be a source of Ti for ilmenite formation.

Geochemical speciation modeling using Geochemist's workbench (GWB standard 14, Aqueous Solutions LLC, Champaign, IL) did not show super-saturation of these minerals. This observation is not surprising considering that our system is heterogeneous due to the presence of minerals and HS. In fact, multiple studies have shown mineral nucleation and growth in under-saturated bulk solutions if organic materials and solid interfaces serve as nucleation templates to locally enrich ions (Deng et al., 2019; Hövelmann et al., 2018; Roberts et al., 2004). For example, Deng et al. (2019) showed barite formation on organic films, despite their bulk solution was under-saturated with respect to barite, likely because of local super-saturation near the organic molecules.

A comparison between LHA and PPHA demonstrated that the treatments with LHA produced more extensive mineralogical transformations, despite its lower EDC and lower extent of Fe(III) reduction (Figs. 1&2). The opposite effect was observed for PPHA, where PPHA reduced more Fe(III), but there was no secondary mineralization . A similar effect was observed in a comparative study between PPHA and AQDS (Liu et al., 2016), where PPHA reduced less Fe(III) in NAu-2 but produced more illite and talc. These results collectively suggest that the roles of HS in electron donation and mineral transformation are not coupled. The electron donating capacity of HS should be related to the phenolic moieties of HS (Aeschbacher et al., 2012; Liu et al., 2017; Ratasuk and Nanny, 2007). However, the role of HS in mineral transformation may be related to their metal complexation ability, which is positively correlated with aromatic carbon content (Fujii et al., 2014). Relative to PPHA, LHA has a higher aromatic carbon (58% versus 47%), aromaticity (0.72 vs. 0.65), and C/H ratio (1.45 vs. 1.23) (Fujii et al., 2014), all of which may have accounted for its stronger role in catalyzing mineral transformation.

676 Furthermore, this decoupling between Fe(III) reduction and mineral transformation
677 suggests that electron transfer from HS to Fe(III) occurred largely in solid state, before
678 dissolution occurred. Otherwise LHA would have reduced more Fe(III), because ligand-
679 and HS-complexed aqueous Fe^{3+} is more reducible than structural Fe(III) in smectite
680 (Kostka et al., 1999) and ferrihydrite (Amstaetter et al., 2012; Nevin and Lovley, 2002).
681 Mineralogical transformation likely occurred after Fe(III) reduction by LHA, because
682 reduced NAu-2 is less stable than un-reduced NAu-2 due to structural dehydroxylation
683 (Stucki et al., 1996).

684 In previous studies on abiotic reduction of Fe oxides by HS (Piepenbrock et al., 2014;
685 Sundman et al., 2017), little mineral transformation occurred, likely because of low HS
686 concentrations used (0.3-0.6 g/L). In this study, with 2.5 g/L, secondary minerals were
687 observed in both abiotic and biotic LHA treatments, but with apparently higher
688 abundance in biotic treatment based on XRD peak intensity (Fig. 5A). Although talc,
689 plagioclase, and illite have been observed individually in previous studies (Liu et al.,
690 2015; Liu et al., 2016), this study observed their co-presence. Because Mg was not
691 present in the bicarbonate buffer, we inferred that Mg in talc may have been derived
692 from NAu-2 or LHA. An insufficient amount of Mg may explain the formation of
693 Fe-containing talc (Figs. 6&7).

694 A two-step mechanism has been proposed previously to explain the HS-promoted talc
695 formation (Liu et al., 2016). In the first step, HS was believed to enhance NAu-2
696 reduction and dissolution, and in the second step, the cations released from NAu-2 (such
697 as Si and Fe) would combine with Mg to precipitate talc. In the presence of microbial
698 cells and their metabolites, mineral precipitation may be facilitated due to the bacterial

699 cell surface and/or metabolic products serving as templates. For example, microbial
700 polysaccharides are believed to template the synthesis of secondary minerals (Chan et al.,
701 2004), especially carboxyl groups that play an important role in mineral crystallization
702 (Konhauser and Urrutia, 1999). In our study, because Mg may be partially derived from
703 LHA (Calvert et al., 1985; Zaccone et al., 2007a), HS may have served as an additional
704 template for talc precipitation.

705 A small amount of ferrihydrite formation (Fig. 8) is unexpected because the overall
706 experimental system was reducing. It may be possible that a small fraction of Fe(III)
707 might be released from HS-induced dissolution of NAu-2, similar to the citrate-induced
708 dissolution of NAu-2 (Liu et al., 2018), and released Fe(III) may form complexes with
709 HS, thus stabilizing such complexed Fe(III) against bioreduction (Maldonado and Price,
710 2001). Ferrihydrite is usually an unstable phase, and over time it should transform to
711 more stable minerals such as goethite (Schwertmann and Murad, 1983). However, the
712 presence of HS may stabilize ferrihydrite, similar to the inhibition of aqueous Fe^{2+}
713 induced transformation of ferrihydrite to crystalline Fe oxides by coprecipitated organic
714 matter (Chen et al., 2015). In this case, organic matter may block the reactive surface
715 sites of ferrihydrite and thus retards its transformation to more stable Fe(III) oxide
716 minerals.

717

718 **IMPLICATIONS**

719 HS are a major organic constituent in peatlands and wetlands, which represent a vast
720 global carbon reservoir (Davidson and Janssens, 2006; Freeman et al., 2004; Rydin and
721 Jeglum, 2013). Our data demonstrated that natural HS can serve as electron donor to

722 reduce structural Fe(III) in clays and promote secondary mineral formation. Although
723 ecologically less relevant concentrations of HS were used in these experiments, given
724 the fact that electron transfer from and to these substances may be reversible (Klüpfel et
725 al., 2014), the accumulative effects of multiple redox cycles of HS may be substantial.
726 Furthermore, in certain peatlands and permafrost (Gentsch et al., 2018; Kirk et al., 2015),
727 organic carbon concentration can be as high as ≥ 12%-20%, which is in a similar range
728 as those used in this study. In such environments, interactions between clay minerals and
729 HS are expected to have an important consequence on Fe redox cycle and mineral
730 transformations.

731 Our data demonstrated the neoformation of talc, albite, illite, and ferrihydrite at the
732 expense of nontronite when humic acids are present in sufficient concentrations. During
733 the dissolution process, nutrients and trace metals may be released into aqueous phase
734 (Rogers and Bennett, 2004) but mineral precipitation would re-sequester them (Donahoe,
735 2004). Because clay minerals have higher surface area and adsorption capacity than
736 secondary minerals, transformations of clays to secondary minerals would result in a
737 decreased surface area and adsorption capacity, thus resulting in an overall release of
738 nutrients, trace metals, and organic carbon. Therefore, investigation of the mutual
739 interactions among clay minerals, organic matter, and microbes is important for
740 understanding soil fertility, nutrient cycling, carbon cycle, and contaminant migration.
741
742
743
744

ACKNOWLEDGEMENTS

This research was supported by a grant from the National Science Foundation (EAR-1656988). A portion of the research was performed at Environmental Molecular Sciences Laboratory (grid. 436923.9), through User Proposal 49851, a DOE Office of Science User Facility sponsored by the Office of Biological and Environmental Research located at PNNL. We are grateful to one anonymous reviewer and Javier Cuadros for their constructive comments which improved the quality of the manuscript.

SUPPLEMENTARY MATERIAL

Supplementary material related to this article can be found online.

REFERENCES CITED

Achal, V., Mukherjee, A., Basu, P.C., and Reddy, M.S. (2009) Lactose mother liquor as an alternative nutrient source for microbial concrete production by Sporosarcina pasteurii. Journal of Industrial Microbiology & Biotechnology, 36(3), 433-438.

Aeschbacher, M., Graf, C., Schwarzenbach, R.P., and Sander, M. (2012) Antioxidant properties of humic substances. Environmental science & technology, 46(9), 4916-4925.

Aeschbacher, M., Sander, M., and Schwarzenbach, R.P. (2010) Novel electrochemical approach to assess the redox properties of humic substances. Environmental science & technology, 44(1), 87-93.

Agangi, A., Reddy, S., Plavsa, D., Vieru, C., Selvaraja, V., LaFlamme, C., Jeon, H., Martin, L., Nozaki, T., and Takaya, Y. (2018) Subsurface deposition of Cu-rich massive sulphide underneath a Palaeoproterozoic seafloor hydrothermal system—the Red Bore prospect, Western Australia. Mineralium Deposita, 1-18.

Aiken, G., McKnight, D., Wershaw, R., and MacCarthy, P. (1985) Humic substances in soil, sediment, and water: geochemistry, isolation, and characterization. Wiley, New York.

Amonette, J.E., and Templeton, J.C. (1998) Improvements to the quantitative assay of nonrefractory minerals for Fe (II) and total Fe using 1, 10-phenanthroline. Clays and Clay Minerals, 46(1), 51-62.

Amstaetter, K., Borch, T., and Kappler, A. (2012) Influence of humic acid imposed changes of ferrihydrite aggregation on microbial Fe (III) reduction. Geochimica et Cosmochimica Acta, 85, 326-341.

Barré, P., Fernandez-Ugalde, O., Virto, I., Velde, B., and Chenu, C. (2014) Impact of phyllosilicate mineralogy on organic carbon stabilization in soils: incomplete knowledge and exciting prospects. Geoderma, 235–236, 382-395.

Bauer, I., and Kappler, A. (2009) Rates and extent of reduction of Fe (III) compounds and O2 by humic substances. Environmental science & technology, 43(13), 4902-4908.

Borden, P.W., Ping, C.-L., McCarthy, P.J., and Naidu, S. (2010) Clay mineralogy in arctic tundra Gelisols, northern Alaska. Soil Science Society of America Journal, 74(2), 580-592.

Bowles, J.F. (1977) A method of tracing the temperature and oxygen-fugacity histories of complex magnetite-ilmenite grains. Mineralogical Magazine, 41(317), 103-109.

Boyanov, M.I., O'Loughlin, E.J., Roden, E.E., Fein, J.B., and Kemner, K.M. (2007) Adsorption of Fe(II) and U(VI) to carboxyl-functionalized microspheres: The influence of speciation on uranyl reduction studied by titration and XAFS. Geochimica et Cosmochimica Acta, 71(8), 1898-1912.

Calvert, S., Mukherjee, S., and Morris, R. (1985) Trace-metals in fulvic and humic acids from modern organic-rich sediments. Oceanologica acta, 8(2), 167-173.

Cao, J., and Jiang, J. (2019) Reducing capacities in continuously released low molecular weight fractions from bulk humic acids. Journal of environmental management, 244, 172-179.

Chan, C.S., De Stasio, G., Welch, S.A., Girasole, M., Frazer, B.H., Nesterova, M.V., Fakra, S., and Banfield, J.F. (2004) Microbial polysaccharides template assembly of nanocrystal fibers. Science, 303(5664), 1656-1658.

Chen, C., Dynes, J.J., Wang, J., and Sparks, D.L. (2014) Properties of Fe-organic matter associations via coprecipitation versus adsorption. Environmental science & technology, 48(23), 13751-13759.

Chen, C., Kukkadapu, R., and Sparks, D.L. (2015) Influence of coprecipitated organic matter on Fe2+ (aq)-catalyzed transformation of ferrihydrite: implications for carbon dynamics. Environmental science & technology, 49(18), 10927-10936.

Coward, E.K., Ohno, T., and Plante, A.F. (2018) Adsorption and Molecular Fractionation of Dissolved Organic Matter on Iron-Bearing Mineral Matrices of Varying Crystallinity. Environmental Science & Technology, 52(3), 1036-1044.

Coward, E.K., Ohno, T., and Sparks, D.L. (2019) Direct Evidence for Temporal Molecular Fractionation of Dissolved Organic Matter at the Iron Oxyhydroxide Interface. Environmental Science & Technology, 53(2), 642-650.

D'Andrilli, J., Chanton, J.P., Glaser, P.H., and Cooper, W.T. (2010) Characterization of dissolved organic matter in northern peatland soil porewaters by ultra high resolution mass spectrometry. Organic Geochemistry, 41(8), 791-799.

Davidson, E.A., and Janssens, I.A. (2006) Temperature sensitivity of soil carbon decomposition and feedbacks to climate change. Nature, 440(7081), 165.

Deng, N., Stack, A.G., Weber, J., Cao, B., De Yoreo, J.J., and Hu, Y. (2019) Organic–mineral interfacial chemistry drives heterogeneous nucleation of Sr-rich (Bax, Sr1− x) SO4 from undersaturated solution. Proceedings of the National Academy of Sciences, 201821065.

Ding, Y., Zhou, Y., Yao, J., Szymanski, C., Fredrickson, J., Shi, L., Cao, B., Zhu, Z., and Yu, X.-Y. (2016) In situ molecular imaging of the biofilm and its matrix. Analytical chemistry, 88(22), 11244-11252.

Dittmar, T., Koch, B., Hertkorn, N., and Kattner, G. (2008) A simple and efficient method for the solid-phase extraction of dissolved organic matter (SPE - DOM) from seawater. Limnology and Oceanography: Methods, 6(6), 230-235.

Donahoe, R.J. (2004) Secondary mineral formation in coal combustion byproduct disposal facilities: implications for trace element sequestration. Geological Society, London, Special Publications, 236(1), 641-658.

Dong, H., Jaisi, D.P., Kim, J., and Zhang, G. (2009) Microbe-clay mineral interactions. American Mineralogist, 94(11-12), 1505-1519.

Dong, H., Kostka, J.E., and Kim, J. (2003) Microscopic Evidence for Microbial Dissolution of Smectite. Clays and Clay Minerals, 51(5), 502-512.

Eusterhues, K., Wagner, F.E., Häusler, W., Hanzlik, M., Knicker, H., Totsche, K.U., Kögel-Knabner, I., and Schwertmann, U. (2008) Characterization of Ferrihydrite-Soil Organic Matter Coprecipitates by X-ray Diffraction and Mössbauer Spectroscopy. Environmental Science & Technology, 42(21), 7891-7897.

Faure, G. (1992) Isotopic records in detrital and authigenic feldspars in sedimentary rocks. Isotopic Signatures and Sedimentary Records, p. 215-238. Springer.

Flerus, R., Koch, B.P., Schmitt-Kopplin, P., Witt, M., and Kattner, G. (2011) Molecular level investigation of reactions between dissolved organic matter and extraction solvents using FT-ICR MS. Marine Chemistry, 124(1-4), 100-107.

Forbes, W.C. (1969) Unit-cell parameters and optical properties of talc on the join Mg3Si4O10 (OH) 2-Fe3Si4O10 (OH) 2. American Mineralogist: Journal of Earth and Planetary Materials, 54(9-10), 1399-1408.

Fredrickson, J.K., Kostandarithes, H.M., Li, S., Plymale, A.E., and Daly, M. (2000) Reduction of fe (III), cr (VI), U (VI), and tc (VII) byDeinococcus radiodurans R1. Applied and environmental microbiology, 66(5), 2006-2011.

Freeman, C., Fenner, N., Ostle, N., Kang, H., Dowrick, D., Reynolds, B., Lock, M., Sleep, D., Hughes, S., and Hudson, J. (2004) Export of dissolved organic carbon from peatlands under elevated carbon dioxide levels. Nature, 430(6996), 195.

Fujii, M., Imaoka, A., Yoshimura, C., and Waite, T. (2014) Effects of molecular composition of natural organic matter on ferric iron complexation at circumneutral pH. Environmental science & technology, 48(8), 4414-4424.

Gates, W., Petit, S., and Madejová, J. (2017) Applications of NIR/MIR to Determine Site Occupancy in Smectites. Developments in Clay Science, 8, p. 200-221. Elsevier.

Gates, W., Slade, P., Manceau, A., and Lanson, B. (2002) Site occupancies by iron in nontronites. Clays and Clay Minerals, 50(2), 223-239.

Gentsch, N., Wild, B., Mikutta, R., Čapek, P., Diáková, K., Schrumpf, M., Turner, S., Minnich, C., Schaarschmidt, F., and Shibistova, O. (2018) Temperature response of permafrost soil carbon is attenuated by mineral protection. Global change biology, 24(8), 3401-3415.

Ghosh, S., Zhen-Yu, W., Kang, S., Bhowmik, P., and Xing, B. (2009) Sorption and fractionation of a peat derived humic acid by kaolinite, montmorillonite, and goethite. Pedosphere, 19(1), 21-30.

Gonsior, M., Peake, B.M., Cooper, W.T., Podgorski, D., D'Andrilli, J., and Cooper, W.J. (2009) Photochemically induced changes in dissolved organic matter identified by ultrahigh resolution Fourier transform ion cyclotron resonance mass spectrometry. Environmental science & technology, 43(3), 698-703.

Gouré-Doubi, H., Martias, C., Smith, A., Villandier, N., Sol, V., Gloaguen, V., and Feuillade, G. (2018) Adsorption of fulvic and humic like acids on surfaces of clays: Relation with SUVA index and acidity. Applied Clay Science.

Gunter, M., Buzon, M., and McNamee, B. (2016) Current Issues with Purported" Asbestos" Content of Talc: Part 1, Introduction and Examples in Metamorphic and Ultramafic Hosted Talc Ores. SME Annual Meeting, p. 8.

Ha, J., Hyun Yoon, T., Wang, Y., Musgrave, C.B., and Brown, J.G.E. (2008) Adsorption of Organic Matter at Mineral/Water Interfaces: 7. ATR-FTIR and Quantum Chemical Study of Lactate Interactions with Hematite Nanoparticles. Langmuir, 24(13), 6683-6692.

Hecht, L., Freiberger, R., Gilg, H.A., Grundmann, G., and Kostitsyn, Y.A. (1999) Rare earth element and isotope (C, O, Sr) characteristics of hydrothermal carbonates: genetic implications for dolomite-hosted talc mineralization at Göpfersgrün (Fichtelgebirge, Germany). Chemical Geology, 155(1-2), 115-130.

Henneberry, Y.K., Kraus, T.E.C., Nico, P.S., and Horwath, W.R. (2012) Structural stability of coprecipitated natural organic matter and ferric iron under reducing conditions. Organic Geochemistry, 48, 81-89.

Hövelmann, J., Putnis, C.V., and Benning, L.G. (2018) Metal sequestration through coupled dissolution–precipitation at the brucite–water interface. Minerals, 8(8), 346.

Howe, H. (2017) The effect of solid solution on the stabilities of selected hydrous phases during subduction. University of Manchester.

Hua, X., Szymanski, C., Wang, Z., Zhou, Y., Ma, X., Yu, J., Evans, J., Orr, G., Liu, S., and Zhu, Z. (2016) Chemical imaging of molecular changes in a hydrated single cell by dynamic secondary ion mass spectrometry and super-resolution microscopy. Integrative Biology, 8(5), 635-644.

Hupp, B.N., and Donovan, J.J. (2018) Quantitative mineralogy for facies definition in the Marcellus Shale (Appalachian Basin, USA) using XRD-XRF integration. Sedimentary Geology, 371, 16-31.

Jaisi, D.P., Kukkadapu, R.K., Eberl, D.D., and Dong, H. (2005) Control of Fe (III) site occupancy on the rate and extent of microbial reduction of Fe (III) in nontronite. Geochimica et Cosmochimica Acta, 69(23), 5429-5440.

Jiang, J., and Kappler, A. (2008) Kinetics of microbial and chemical reduction of humic substances: implications for electron shuttling. Environmental science & technology, 42(10), 3563-3569.

Kappler, A., Benz, M., Schink, B., and Brune, A. (2004) Electron shuttling via humic acids in microbial iron (III) reduction in a freshwater sediment. FEMS Microbiology Ecology, 47(1), 85-92.

Keeling, J.L., Raven, M.D., and Gates, W.P. (2000) Geology and characterization of two hydrothermal nontronites from weathered metamorphic rocks at the Uley graphite mine, South Australia. Clays and Clay Minerals, 48(5), 537-548.

Kirk, E.R., van Kessel, C., Horwath, W.R., and Linquist, B.A. (2015) Estimating annual soil carbon loss in agricultural peatland soils using a nitrogen budget approach. PloS one, 10(3).

Kleber, M., and Lehmann, J. (2019) Humic substances extracted by alkali are invalid proxies for the dynamics and functions of organic matter in terrestrial and aquatic ecosystems. Journal of Environmental Quality, 48(2), 207-216.

Klüpfel, L., Piepenbrock, A., Kappler, A., and Sander, M. (2014) Humic substances as fully regenerable electron acceptors in recurrently anoxic environments. Nature Geoscience, 7(3), 195.

Koch, B., and Dittmar, T. (2006) From mass to structure: An aromaticity index for high-resolution mass data of natural organic matter. Rapid communications in mass spectrometry, 20(5), 926-932.

Koch, B.P., Witt, M., Engbrodt, R., Dittmar, T., and Kattner, G. (2005) Molecular formulae of marine and terrigenous dissolved organic matter detected by electrospray ionization Fourier transform ion cyclotron resonance mass spectrometry. Geochimica et Cosmochimica Acta, 69(13), 3299-3308.

Konhauser, K.O., and Urrutia, M.M. (1999) Bacterial clay authigenesis: a common biogeochemical process. Chemical Geology, 161(4), 399-413.

Kostka, J.E., Haefele, E., Viehweger, R., and Stucki, J.W. (1999) Respiration and dissolution of iron (III)-containing clay minerals by bacteria. Environmental Science & Technology, 33(18), 3127-3133.

Kujawinski, E.B., and Behn, M.D. (2006) Automated analysis of electrospray ionization Fourier transform ion cyclotron resonance mass spectra of natural organic matter. Analytical Chemistry, 78(13), 4363-4373.

Kursun, H., and Ulusoy, U. (2006) Influence of shape characteristics of talc mineral on the column flotation behavior. International Journal of Mineral Processing, 78(4), 262-268.

Lehmann, J., and Kleber, M. (2015) The contentious nature of soil organic matter. Nature, 528(7580), 60.

Liu, D., Dong, H., Wang, H., and Zhao, L. (2015) Low-temperature feldspar and illite formation through bioreduction of Fe(III)-bearing smectite by an alkaliphilic bacterium. Chemical Geology, 406, 25-33.

Liu, D., Zhang, Q., Wu, L., Zeng, Q., Dong, H., Bishop, M.E., and Wang, H. (2016) Humic acid-enhanced illite and talc formation associated with microbial reduction of Fe (III) in nontronite. Chemical Geology, 447, 199-207.

Liu, G., Qiu, S., Liu, B., Pu, Y., Gao, Z., Wang, J., Jin, R., and Zhou, J. (2017) Microbial reduction of Fe (III)-bearing clay minerals in the presence of humic acids. Scientific reports, 7, 45354.

Liu, X., Dong, H., Yang, X., Kovarik, L., Chen, Y., and Zeng, Q. (2018) Effects of citrate on hexavalent chromium reduction by structural Fe (II) in nontronite. Journal of hazardous materials, 343, 245-254.

Lovley, D., Fraga, J., Blunt-Harris, E., Hayes, L., Phillips, E., and Coates, J. (1998) Humic substances as a mediator for microbially catalyzed metal reduction. Acta hydrochimica et hydrobiologica, 26(3), 152-157.

Lovley, D.R., Coates, J.D., Blunt-Harris, E.L., Phillips, E.J., and Woodward, J.C. (1996) Humic substances as electron acceptors for microbial respiration. Nature, 382(6590), 445.

Lovley, D.R., Fraga, J.L., Coates, J.D., and Blunt-Harris, E.L. (1999) Humics as an electron donor for anaerobic respiration. Environmental Microbiology, 1(1), 89-98.

Lv, J., Zhang, S., Wang, S., Luo, L., Cao, D., and Christie, P. (2016) Molecular-scale investigation with ESI-FT-ICR-MS on fractionation of dissolved organic matter induced by adsorption on iron oxyhydroxides. Environmental science & technology, 50(5), 2328-2336.

Maldonado, M.T., and Price, N.M. (2001) Reduction and transport of organically bound iron by Thalassiosira oceanica (Bacillariophyceae). Journal of Phycology, 37(2), 298-310.

Mejia, J., He, S., Yang, Y., Ginder-Vogel, M., and Roden, E.E. (2018) Stability of Ferrihydrite–Humic Acid Coprecipitates under Iron-Reducing Conditions. Environmental Science & Technology, 52(22), 13174-13183.

Michel, F.M., Ehm, L., Antao, S.M., Lee, P.L., Chupas, P.J., Liu, G., Strongin, D.R., Schoonen, M.A., Phillips, B.L., and Parise, J.B. (2007) The structure of ferrihydrite, a nanocrystalline material. Science, 316(5832), 1726-1729.

Minor, E.C., Steinbring, C.J., Longnecker, K., and Kujawinski, E.B. (2012) Characterization of dissolved organic matter in Lake Superior and its watershed using ultrahigh resolution mass spectrometry. Organic Geochemistry, 43, 1-11.

Nevin, K.P., and Lovley, D.R. (2002) Mechanisms for Fe (III) oxide reduction in sedimentary environments. Geomicrobiology Journal, 19(2), 141-159.

Pentráková, L., Su, K., Pentrák, M., and Stucki, J. (2013) A review of microbial redox interactions with structural Fe in clay minerals. Clay Minerals, 48(3), 543-560.

Perdue, E.M., Gjessing, E.T., and Glaze, W. (1990) Organic acids in aquatic ecosystems. Dahlem Workshop on Organic Acids in Aquatic Ecosystems (1989: Berlin, Germany). Wiley.

Peretyazhko, T., and Sposito, G. (2006) Reducing capacity of terrestrial humic acids. Geoderma, 137(1-2), 140-146.

Petruk, W., Farrell, D., Laufer, E., Tremblay, R., and Manning, P. (1977) Nontronite and ferruginous opal from the Peace River iron deposit in Alberta, Canada. Canadian Mineralogist, 15(1), 14-21.

Piepenbrock, A., Dippon, U., Porsch, K., Appel, E., and Kappler, A. (2011) Dependence of microbial magnetite formation on humic substance and ferrihydrite concentrations. Geochimica et Cosmochimica Acta, 75(22), 6844-6858.

Piepenbrock, A., Schröder, C., and Kappler, A. (2014) Electron transfer from humic substances to biogenic and abiogenic Fe (III) oxyhydroxide minerals. Environmental science & technology, 48(3), 1656-1664.

Ratasuk, N., and Nanny, M.A. (2007) Characterization and quantification of reversible redox sites in humic substances. Environmental Science & Technology, 41(22), 7844-7850.

Reza, A.S., Jean, J.-S., Lee, M.-K., Kulp, T.R., Hsu, H.-F., Liu, C.-C., and Lee, Y.-C. (2012) The binding nature of humic substances with arsenic in alluvial aquifers of Chianan Plain, southwestern Taiwan. Journal of Geochemical Exploration, 114, 98-108.

Roberts, J.A., Bennett, P.C., González, L.A., Macpherson, G., and Milliken, K.L. (2004) Microbial precipitation of dolomite in methanogenic groundwater. Geology, 32(4), 277-280.

Rogers, J.R., and Bennett, P.C. (2004) Mineral stimulation of subsurface microorganisms: release of limiting nutrients from silicates. Chemical Geology, 203(1-2), 91-108.

Rosario-Ortiz, F. (2015) Advances in the physicochemical characterization of dissolved organic matter: impact on natural and engineered systems. Oxford University Press.

973 Roth, V.-N., Dittmar, T., Gaupp, R., and Gleixner, G. (2013) Latitude and pH driven trends in the
974 molecular composition of DOM across a north south transect along the Yenisei River. Geochimica et
975 Cosmochimica Acta, 123, 93-105.
976 Rydin, H., and Jeglum, J.K. (2013) The biology of peatlands, 2e. Oxford university press.
977 Saidy, A.R., Smernik, R.J., Baldock, J.A., Kaiser, K., Sanderman, J., and Macdonald, L.M. (2012) Effects
978 of clay mineralogy and hydrous iron oxides on labile organic carbon stabilisation. Geoderma,
979 173–174, 104-110.
980 Sánchez-Cortés, S., Francioso, O., Ciavatta, C., Garcıa-Ramos, J., and Gessa, C. (1998) pH-dependent
981 adsorption of fractionated peat humic substances on different silver colloids studied by
982 surface-enhanced Raman spectroscopy. Journal of Colloid and interface Science, 198(2), 308-318.
983 Schwertmann, U., and Murad, E. (1983) Effect of pH on the formation of goethite and hematite from
984 ferrihydrite. Clays and Clay Minerals, 31(4), 277-284.
985 Seifert, A.-G., Roth, V.-N., Dittmar, T., Gleixner, G., Breuer, L., Houska, T., and Marxsen, J. (2016)
986 Comparing molecular composition of dissolved organic matter in soil and stream water: Influence of
987 land use and chemical characteristics. Science of the Total Environment, 571, 142-152.
988 Shimizu, M., Zhou, J., Schröder, C., Obst, M., Kappler, A., and Borch, T. (2013) Dissimilatory Reduction
989 and Transformation of Ferrihydrite-Humic Acid Coprecipitates. Environmental Science &
990 Technology, 47(23), 13375-13384.
991 Sleighter, R.L., and Hatcher, P.G. (2008) Molecular characterization of dissolved organic matter (DOM)
992 along a river to ocean transect of the lower Chesapeake Bay by ultrahigh resolution electrospray
993 ionization Fourier transform ion cyclotron resonance mass spectrometry. Marine chemistry, 110(3-4),
994 140-152.
995 Sleighter, R.L., Liu, Z., Xue, J., and Hatcher, P.G. (2010) Multivariate statistical approaches for the
996 characterization of dissolved organic matter analyzed by ultrahigh resolution mass spectrometry.
997 Environmental science & technology, 44(19), 7576-7582.
998 Sowers, T.D., Holden, K.L., Coward, E.K., and Sparks, D.L. (2019a) Dissolved organic matter sorption
999 and molecular fractionation by naturally-occurring bacteriogenic iron (oxyhydr) oxides. Environmental
1000 Science & Technology.
1001 -. (2019b) Dissolved Organic Matter Sorption and Molecular Fractionation by Naturally Occurring
1002 Bacteriogenic Iron (Oxyhydr) oxides. Environmental science & technology, 53(8), 4295-4304.
1003 Stern, N., Mejia, J., He, S., Yang, Y., Ginder-Vogel, M., and Roden, E.E. (2018) Dual role of humic
1004 substances as electron donor and shuttle for dissimilatory iron reduction. Environmental science &
1005 technology, 52(10), 5691-5699.
1006 Stucki, J.W., Bailey, G.W., and Gan, H. (1996) Oxidation-reduction mechanisms in iron-bearing
1007 phyllosilicates. Applied Clay Science, 10(6), 417-430.
1008 Stucki, J.W., and Kostka, J.E. (2006) Microbial reduction of iron in smectite. Comptes Rendus
1009 Geoscience, 338(6-7), 468-475.
1010 Sundman, A., Byrne, J.M., Bauer, I., Menguy, N., and Kappler, A. (2017) Interactions between magnetite
1011 and humic substances: redox reactions and dissolution processes. Geochemical transactions, 18(1), 6.
1012 Sutton, R., and Sposito, G. (2005) Molecular structure in soil humic substances: the new view.
1013 Environmental science & technology, 39(23), 9009-9015.
1014 Theng, B.K.G. (1976) Interactions between montmorillonite and fulvic acid. Geoderma, 15(3), 243-251.
1015 Tolić, N., Liu, Y., Liyu, A., Shen, Y., Tfaily, M.M., Kujawinski, E.B., Longnecker, K., Kuo, L.-J.,
1016 Robinson, E.W., and Paša-Tolić, L. (2017) Formularity: software for automated formula assignment of
1017 natural and other organic matter from ultrahigh-resolution mass spectra. Analytical Chemistry, 89(23),
1018 12659-12665.
1019 Vermeer, A.W.P., van Riemsdijk, W.H., and Koopal, L.K. (1998) Adsorption of Humic Acid to Mineral
1020 Particles. 1. Specific and Electrostatic Interactions. Langmuir, 14(10), 2810-2819.
1021 Waggoner, D.C., and Hatcher, P.G. (2017) Hydroxyl radical alteration of HPLC fractionated lignin:
1022 Formation of new compounds from terrestrial organic matter. Organic Geochemistry, 113, 315-325.
1023 Wang, K., and Xing, B. (2005) Structural and sorption characteristics of adsorbed humic acid on clay
1024 minerals. Journal of Environmental Quality, 34(1), 342-349.
1025 Weber, K.A., Achenbach, L.A., and Coates, J.D. (2006) Microorganisms pumping iron: anaerobic
1026 microbial iron oxidation and reduction. Nature Reviews Microbiology, 4(10), 752-764.
1027 Weber, K.A., Picardal, F.W., and Roden, E.E. (2001) Microbially catalyzed nitrate-dependent oxidation of
1028 biogenic solid-phase Fe (II) compounds. Environmental Science & Technology, 35(8), 1644-1650.

Xu, L., Peng, T., Tian, J., Lu, Z., Hu, Y., and Sun, W. (2017) Anisotropic surface physicochemical properties of spodumene and albite crystals: Implications for flotation separation. Applied Surface Science, 426, 1005-1022.

Yang, J., Kukkadapu, R.K., Dong, H., Shelobolina, E.S., Zhang, J., and Kim, J. (2012) Effects of redox cycling of iron in nontronite on reduction of technetium. Chemical Geology, 291, 206-216.

Yang, Z., Kappler, A., and Jiang, J. (2016) Reducing capacities and distribution of redox-active functional groups in low molecular weight fractions of humic acids. Environmental science & technology, 50(22), 12105-12113.

Zaccone, C., Cocozza, C., Cheburkin, A., Shotyk, W., and Miano, T. (2007a) Enrichment and depletion of major and trace elements, and radionuclides in ombrotrophic raw peat and corresponding humic acids. Geoderma, 141(3-4), 235-246.

Zaccone, C., Cocozza, C., D'orazio, V., Plaza, C., Cheburkin, A., and Miano, T. (2007b) Influence of extractant on quality and trace elements content of peat humic acids. Talanta, 73(5), 820-830.

Zhang, L., Luo, L., and Zhang, S. (2012) Integrated investigations on the adsorption mechanisms of fulvic and humic acids on three clay minerals. Colloids and Surfaces A: Physicochemical and Engineering Aspects, 406, 84-90.

Zhao, L., Dong, H., Kukkadapu, R., Agrawal, A., Liu, D., Zhang, J., and Edelmann, R.E. (2013) Biological oxidation of Fe (II) in reduced nontronite coupled with nitrate reduction by Pseudogulbenkiania sp. strain 2002. Geochimica et Cosmochimica Acta, 119, 231-247.

Zhao, L., Dong, H., Kukkadapu, R.K., Zeng, Q., Edelmann, R.E., Pentrák, M., and Agrawal, A. (2015) Biological Redox Cycling of Iron in Nontronite and Its Potential Application in Nitrate Removal. Environmental Science & Technology, 49(9), 5493-5501.

Zheng, X., Liu, Y., Fu, H., Qu, X., Yan, M., Zhang, S., and Zhu, D. (2019) Comparing electron donating/accepting capacities (EDC/EAC) between crop residue-derived dissolved black carbon and standard humic substances. Science of the Total Environment, 673, 29-35.

This is the peer-reviewed, final accepted version for American Mineralogist, published by the Mineralogical Society of America.
The published version is subject to change. Cite as Authors (Year) Title. American Mineralogist, in press.
DOI: https://doi.org/10.2138/am-2021-7828. http://www.minsocam.org/

1056 **Table 1** The conditions of experiments and analytical methods performed

	Non-growth condition	Growth condition
Medium	Bicarbonate buffer	Growth medium
Bioreduction experiment	✓	✓
Supplementary experiment		✓
Production of Fe(II) over time	✓	✓
EDC		✓
FT-ICR-MS	✓	✓
Analysis of the solids (FTIR, ToF-SIMS, XRD, SEM, and TEM)	✓	

1057 Bicarbonate buffer: $NaHCO_3$ (29.76 mM), KCl (1.34 mM), pH 7.0
1058 Growth medium: NH_4Cl (4.67 mM), KH_2PO_4 (4.41 mM), KCl (1.34 mM), $NaHCO_3$ (29.76 mM), Wolfe's
1059 Mineral solution (10 ml/L) and Wolfe's vitamin solution (10 ml/L), pH 7.0.
1060

1061 **Table 2** Magnitude-weighted parameters for all formulas for samples in growth medium

1062 at 2.5 g/L concentration

	LHA GROUP				PPHA GROUP			
	LHA control	NAu-2&LHA	NAu-2&LHA &CN32	% Change (w.r.t. control)	PPHA control	NAu-2&PPHA	NAu-2&PPHA &CN32	% Change (w.r.t. control)
$(DBE)_w$	14.827	14.862	14.678	1	13.949	14.093	13.613	2
stdev	0.003	0.003	0.003		0.002	0.002	0.002	
$(DBE/O)_w$	1.520	1.526	1.494	2	1.384	1.368	1.337	3
stdev	0.000	0.000	0.000		0.000	0.000	0.000	
$(DBE-O)_w$	4.333	4.445	4.204	3	3.288	3.297	2.967	10
stdev	0.001	0.001	0.001		0.001	0.001	0.001	
$(AI)_w$	0.366	0.380	0.359	2	0.276	0.277	0.240	13
stdev	0.000	0.000	0.000		0.000	0.000	0.000	

1063
1064
1065

Figure captions

Fig. 1. Time-course changes of concentration of total Fe(II) in the clay suspensions as measured by the 1,10-phenanthroline method. Fig. A represents the LHA group and B represents the PPHA group in bicarbonate buffer. The error bars in A-D are from duplicate experiments.

Fig. 2. Time-course changes of concentration of total Fe(II) in the suspensions as measured by the 1,10-phenanthroline method and EDC values for samples in growth medium. (A & C) represent the LHA group, and (B & D) represent the PPHA group. (A & B) show Fe(II) production for various controls and treatments. (C & D) show comparisons in Fe(III) reduction by pre-reduced (by *S. putrefaciens* CN32) and native HS. (E) shows the changes in Electron Donating Capacity (EDC) between HS controls and treated samples (2.5 g/L concentration). The error bars in A-D are from duplicate experiments, and those in E are from triplicate analyses.

Fig. 3. Fourier-transform infrared (FTIR) spectra in the wavenumber range of 1800-1100 cm^{-1} showing N-H and $R\text{-}COO^{-}$ bending vibration bands. Pure LHA/PPHA/NAu-2 controls were superimposed on top of samples for comparison. LHA/PPHA peak identification was adopted from International Humic Substances Society (http://humic-substances.org/) and NAu-2 adopted from a previous study (Petruk et al., 1977). The numbers on the figure note the peak position.

Fig. 4. Scores and loadings plot of the two principal component analysis of

time-of-flight secondary-ion mass spectrometry (ToF-SIMS) spectra data collected in negative mode. (A) Spectral PCA scores plot of LHA (squares) and PPHA groups (circles). (B) Loadings plot of PC1 showing distributions of different ions in positive and negative values. (C) Loadings plot of PC2 showing distributions of different ions in positive and negative values.

Fig. 5. X-ray diffraction patterns for NAu-2 control and HA-CN32 treated NAu-2 samples. (A) Leonardite humic acid (LHA) groups incubated for 1 month showing emergence of new peaks (denoted with arrows) in reduced samples. (B) XRD patterns for air-dried and ethylene glycolated Leonardite humic acid (LHA) groups that were incubated for 9 months, showing the presence of the two strongest peaks of talc (JCPDS #19-0770) and the strongest peak of albite (JCPDS #10-0393); (C) Pahokee Peat humic acid (PPHA) treatment groups showing no detectable difference in mineralogy among different samples.

Fig. 6. SEM images showing the formation of new minerals as a result of LHA and live cell treatment; (A) Original NAu-2 sample with a typical nontronite composition; (B) An illite-smectite (I-S) particle showing a platy structure (white arrow) and CN32 cells (white oval). EDS composition of the I-S particle shows a small K peak. (C) Neoformed silica particle (white arrow) with Si and O peaks in the EDS spectrum and black arrow denotes ilmenite with an EDS spectrum showing O, Fe, and Ti. CN32 cells (white oval) are in the same field of view as neoformed silica and ilmenite particles; (D) A typical albite crystal with Na, Ca, Al, and Si as major elements; (E) Fibrous talc particles (white

arrow) along with a plate-like albite particle. The talc exhibits a typical composition (e.g., Mg and Si with some Fe); (F) A talc particle showing a layered texture with a similar composition but with some Ca and Al. In all EDS spectra, the Au peak is from Au coating. The C peak should be derived from bicarbonate buffer and LHA.

Fig. 7. Talc identification by TEM observation and EDS analysis of the LHA-NAu-2-CN32 sample. (A) A low magnification TEM image of a talc particle displaying a layered structure with a size ~1.8 μm × 2.4 μm; (B) An enlarged TEM image displaying an edge of the particle in A (white square), showing lattice fringes, however, it was difficult to acquire a high magnification lattice fringe image due to the large thickness; (C) SAED pattern of the corresponding area in (B) showing a pseudo-hexagonal electron diffraction pattern when taken along the [001] zone axis;
(D) Corresponding EDS spectrum of talc in A showing a typical composition but with enriched Fe.

Fig. 8. Authigenic ilmenite and ferrihydrite as observed under TEM and their corresponding EDS spectra. (A) A low magnification TEM image showing sharp edges of an ilmenite particle; (B) A high resolution TEM image of the squared area in A, showing 0.25 nm and 0.27 nm lattice fringes for (-1 2 0) and (1 0 4) reflections, respectively; (C) A corresponding EDS spectrum of the ilmenite particle of the squared area in A, showing a typical composition of Fe, Ti and O. (D) A SAED pattern of ilmenite and ferrihydrite mixture. There appears to be three sets of SAED patterns superimposed onto one another: 1) the reflections of one single crystal of ferrihydrite

1135 (indexed, along the [0 -2 0] zone axis); 2) polycrystalline ferrihydrite; 3) ilmenite single
1136 crystal patterns. (2) and (3) are not indexed for clarity. (E) A SAED pattern of
1137 polycrystalline ferrihydrite showing concentric rings. (F) An ilmenite single crystal
1138 SAED pattern taken along the [4 2 -1] zone axis.
1139

This is the peer-reviewed, final accepted version for American Mineralogist, published by the Mineralogical Society of America.
The published version is subject to change. Cite as Authors (Year) Title. American Mineralogist, in press.
DOI: https://doi.org/10.2138/am-2021-7828. http://www.minsocam.org/

1140

1141

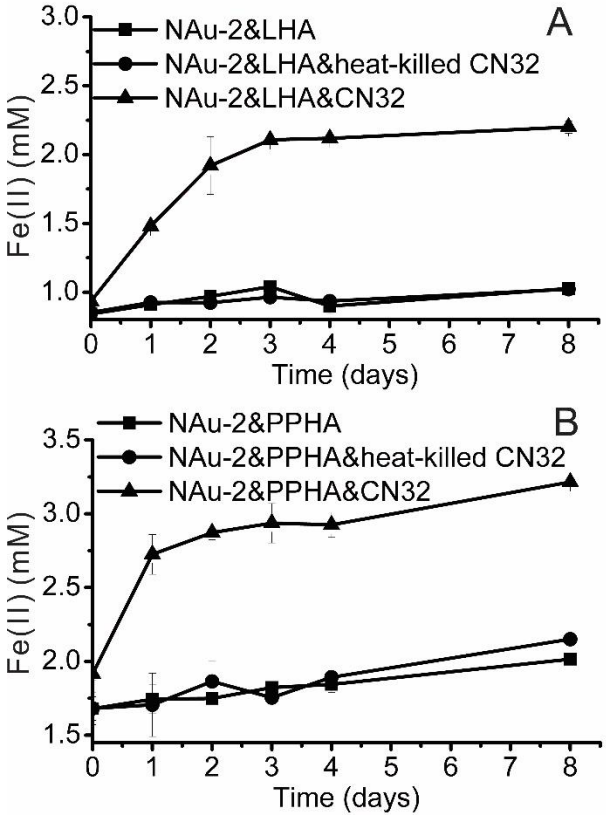

1142
1143 **Fig. 1.**
1144

This is the peer-reviewed, final accepted version for American Mineralogist, published by the Mineralogical Society of America.
The published version is subject to change. Cite as Authors (Year) Title. American Mineralogist, in press.
DOI: https://doi.org/10.2138/am-2021-7828. http://www.minsocam.org/

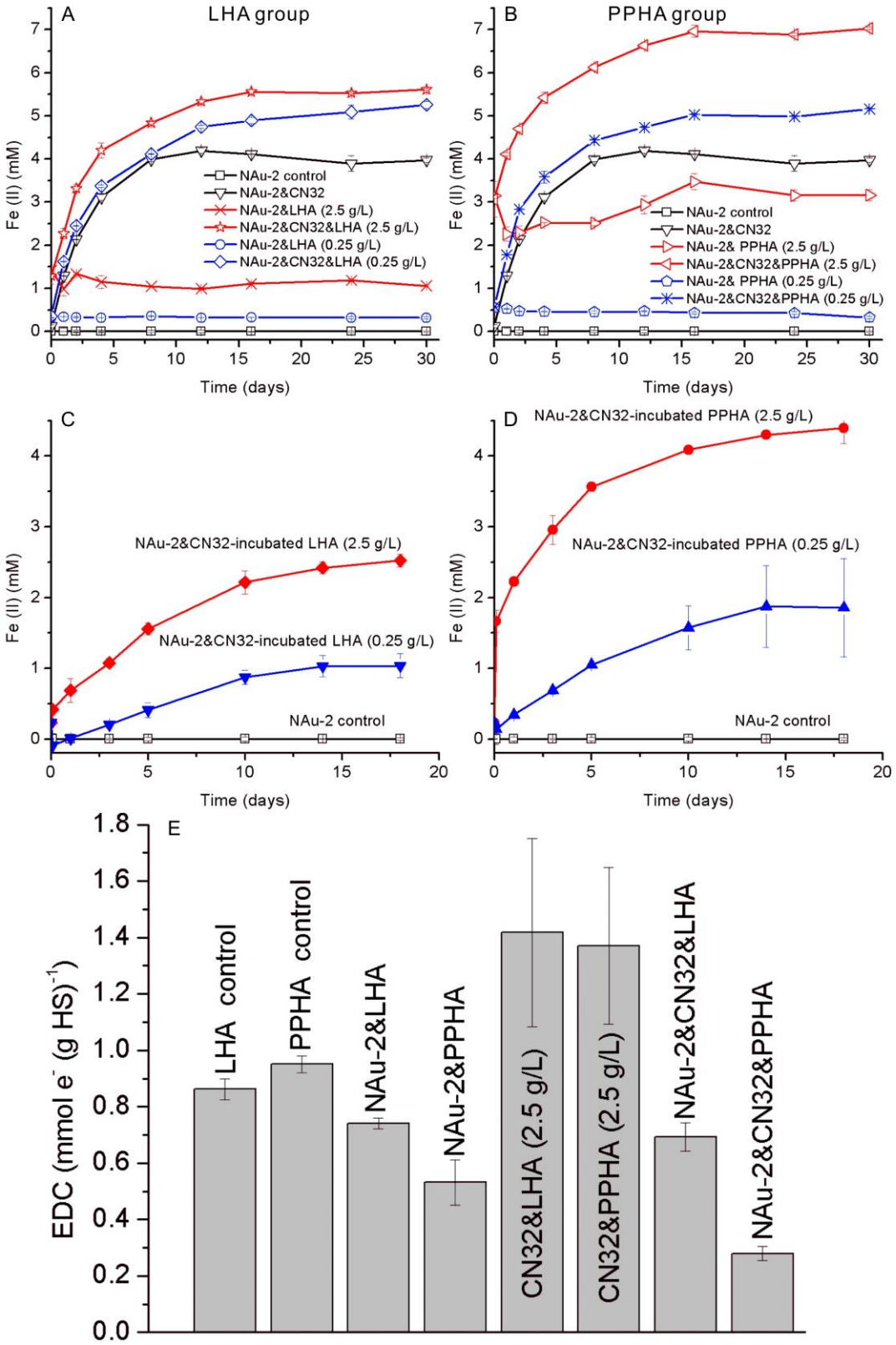

Fig. 2.

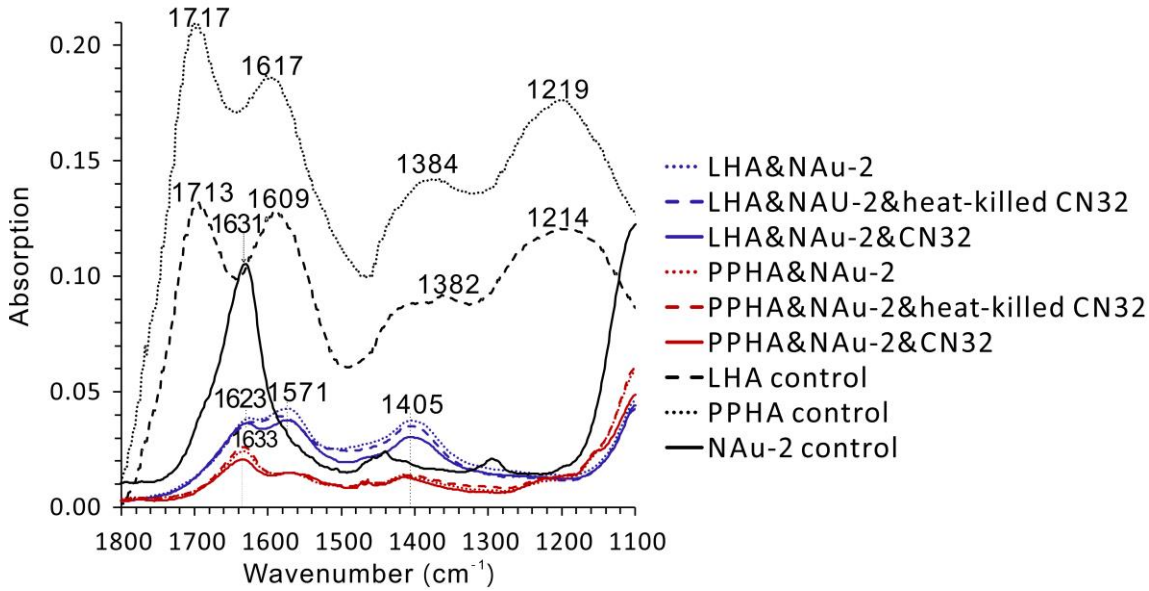

Fig. 3.

This is the peer-reviewed, final accepted version for American Mineralogist, published by the Mineralogical Society of America.
The published version is subject to change. Cite as Authors (Year) Title. American Mineralogist, in press.
DOI: https://doi.org/10.2138/am-2021-7828. http://www.minsocam.org/

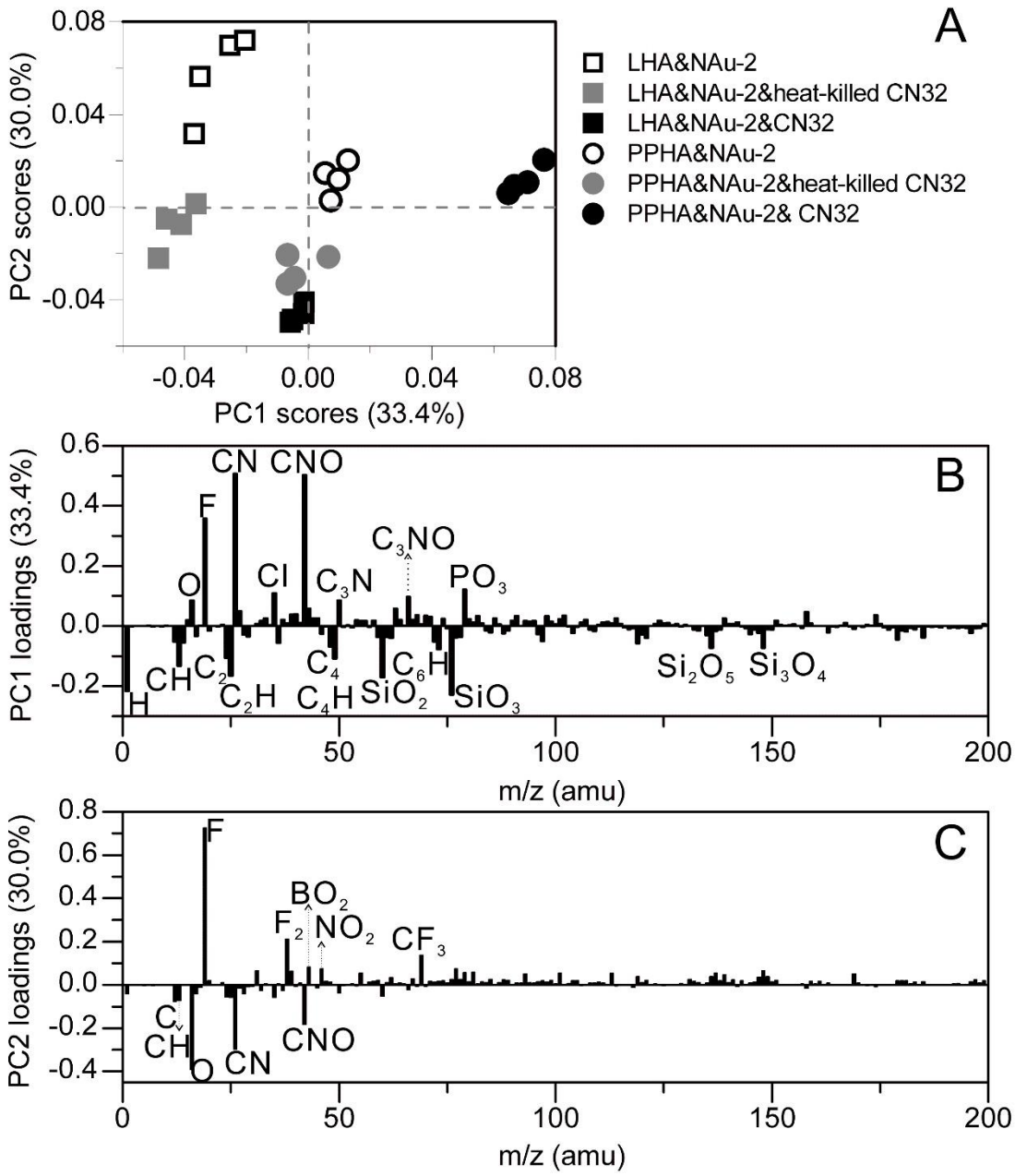

Fig. 4.

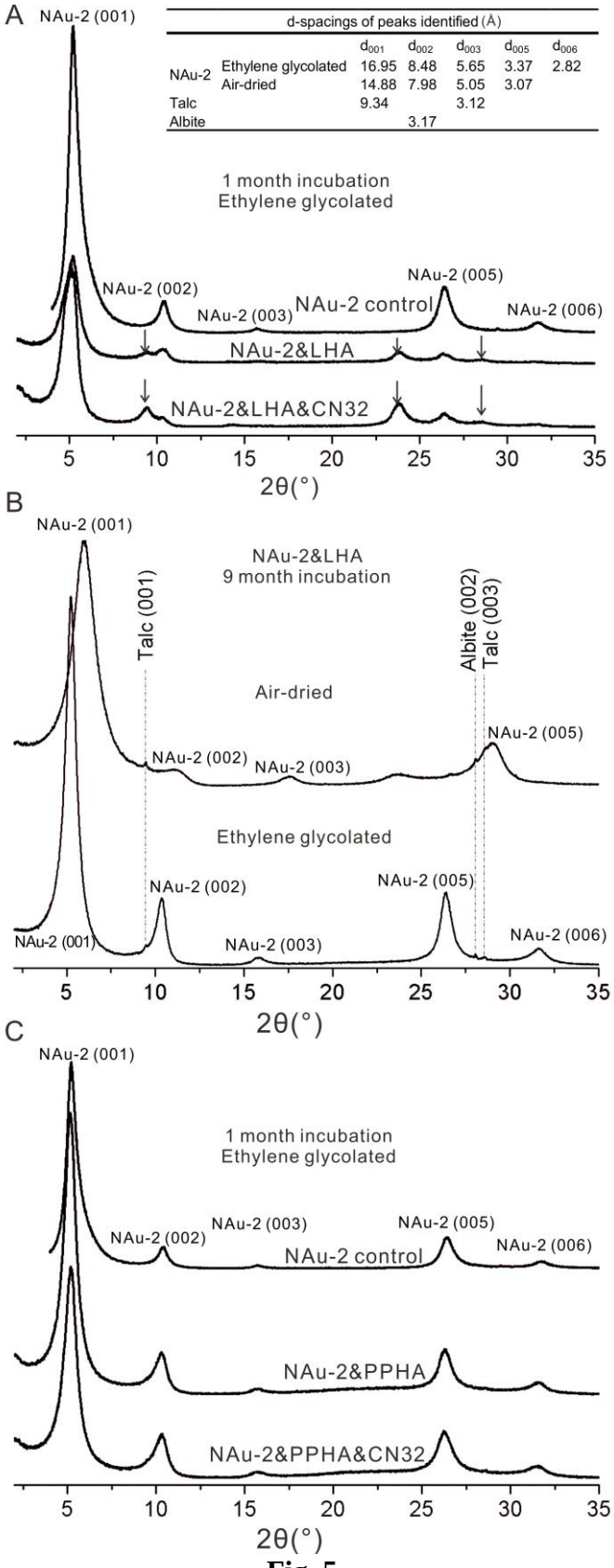

Fig. 5.

This is the peer-reviewed, final accepted version for American Mineralogist, published by the Mineralogical Society of America.
The published version is subject to change. Cite as Authors (Year) Title. American Mineralogist, in press.
DOI: https://doi.org/10.2138/am-2021-7828. http://www.minsocam.org/

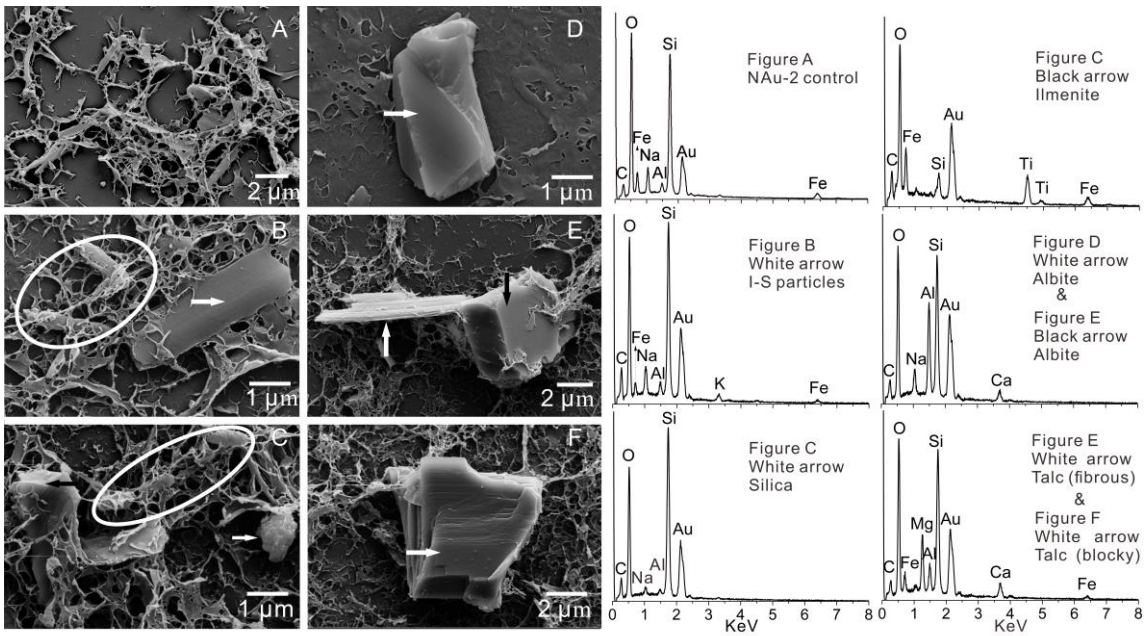

Fig. 6.

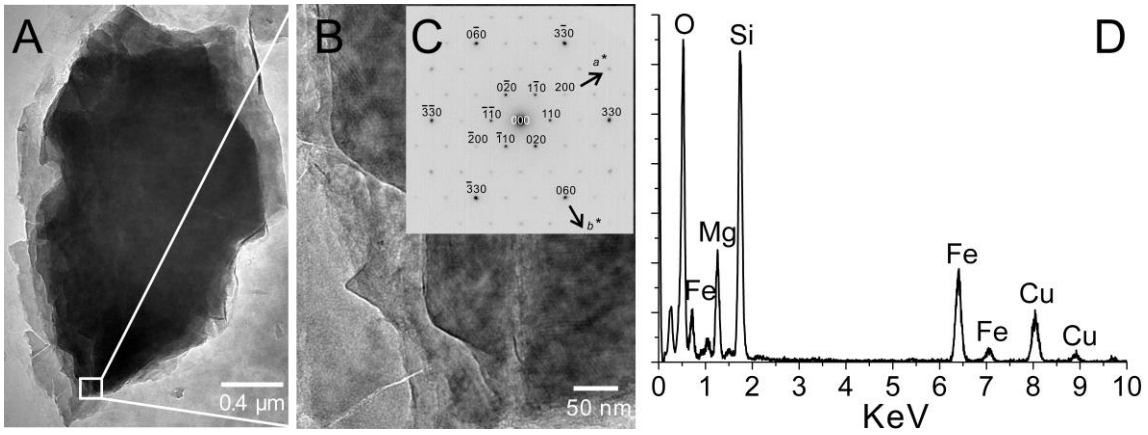

Fig. 7.

This is the peer-reviewed, final accepted version for American Mineralogist, published by the Mineralogical Society of America.
The published version is subject to change. Cite as Authors (Year) Title. American Mineralogist, in press.
DOI: https://doi.org/10.2138/am-2021-7828. http://www.minsocam.org/

1171

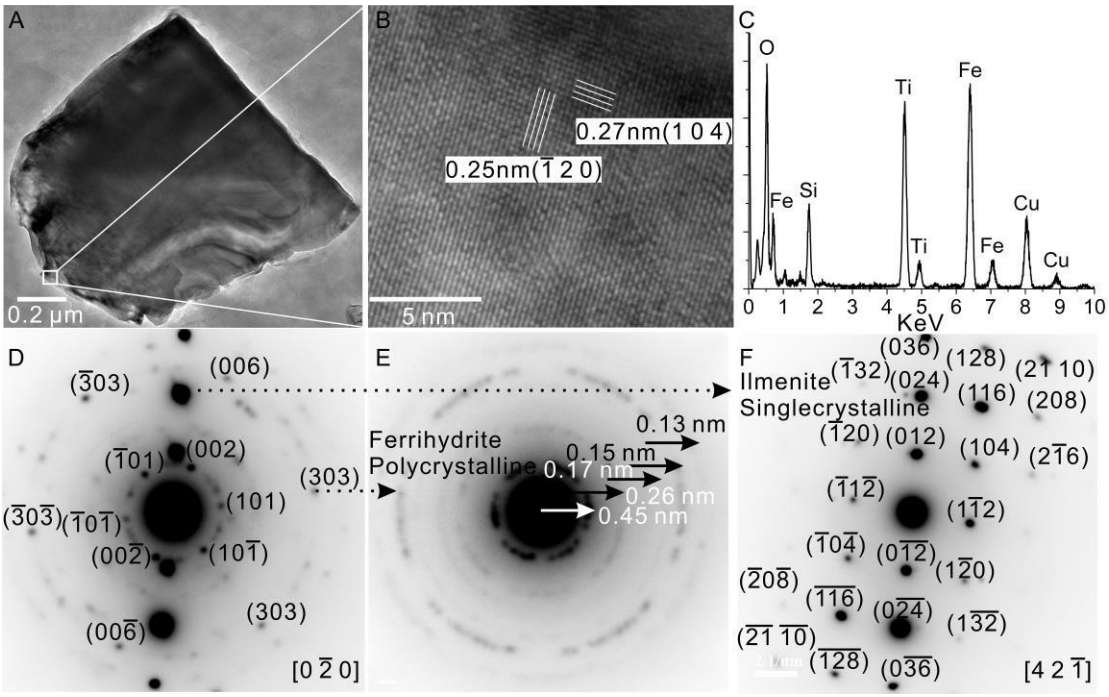

1172

1173 **Fig. 8.**